https://doi.org/10.1016/j.cma.2020.113507

Adjusting fictitious domain parameters for fairly priced image-based modeling: Application to the regularization of Digital Image Correlation

Ali Rouwane[a,b,*], Robin Bouclier[a,b], Jean-Charles Passieux[a], Jean-Noël Périé[a]

[a] *Institut Clément Ader (ICA), Université de Toulouse, INSA-ISAE-Mines Albi-UPS-CNRS, Toulouse, France*
[b] *Institut de Mathématiques de Toulouse (IMT), Université de Toulouse, UPS-UT1-UT2-INSA-CNRS, Toulouse, France*

Abstract

The integration of numerical simulation and experimental measurements in cellular materials at the sub-cellular scale is a real challenge. On the experimental side, the almost absence of texture makes displacement fields measurement tricky. On the simulation side, it requires the construction of reliable and specimen-specific geometric and mechanical models from digital images. For this purpose, high order based fictitious domain approaches have proven to be an efficient alternative to boundary conforming finite elements for the analysis of geometrically complex objects. A number of discretization parameters needs to be set by the user by making a trade-off between accuracy and computational cost. In addition to numerical errors (interpolation, integration *etc.*), there are additional geometric and model errors due to the pixelation of the image (*e.g.*, quantization, sampling, noise). In the literature, discretization parameters are often analyzed without taking pixelation into account, which can lead to over-calculations. In this paper, these parameters are adjusted to obtain (a) the best possible accuracy (bounded by pixelation errors) while (b) ensuring minimal complexity (concept of fair price). In order to analyze the different sources of error, various two-dimensional synthetic experiments are generated by mimicking the image acquisition process from high-resolution numerical simulations considered as a reference. The approach leads to a modeling that outperforms conventional approaches both in terms of accuracy and complexity. Eventually, it is shown that the presented image-based models provide a unique opportunity to assist digital volume correlation and allow the measurement of relevant local kinematics within cellular materials.

Keywords: Image-based models, Isogeometric analysis, Immersed boundary methods, B-splines, Cellular materials, Elastic image registration.

1. Introduction

Recent advances in micro-tomography provide a unique opportunity to characterize and model the behavior of architectured materials [1]. On the one hand, the acquired volumetric images can be used to build fine Finite Element Digital Image-Based (FE-DIB) models that account for the architecture [2, 3, 4] or even the micro-structure [5, 6, 7, 8, 9, 10, 11, 12]. On the other hand, the addition of specific experimental test means makes it possible to study the behavior of the material *in situ* [13]. Within this context, Digital Volume Correlation (DVC) aims at measuring full field volume displacement fields at several loadings [14].

Concerning the image-based model aspect, multiple approaches are conceivable. A voxel-based hexahedron mesh has the merit of being immediate to build [15]. It should be noted that one could hope avoiding the segmentation step by using the gray-level value to adjust the voxel behavior [16]. However, such a structured mesh may generate unphysical stress concentrations [2]. In addition, such approaches usually lead to huge FE problems and excessive computational burdens which require the development of

*Corresponding author
Email addresses: ali.rouwane@univ-tlse3.fr (Ali Rouwane), bouclier@insa-toulouse.fr (Robin Bouclier), passieux@insa-toulouse.fr (Jean-Charles Passieux), jean-noel.perie@iut-tlse3.fr (Jean-Noël Périé)

specific high performance computing tools [17, 12]. An alternative is to construct a tetrahedron based FE mesh that conforms to the architecture [18]. The automation of such a procedure is still not obvious and the size of the problem to be solved remains a real bottleneck. As a result, a current trend in the field of image-based models consists in resorting to fictitious domain type approaches that offer the opportunity to dissociate the shape function basis from the actual geometry [19, 8, 9, 10, 20]. More precisely, when combined with higher order and regular functions, these embedded domain (also referred to as immersed boundary, or unfitted, or even cut) finite-element techniques seem to meet their full potential. In fact, they allow for an accurate description of the mechanical fields while saving a large amount of degrees of freedom compared to standard low-order boundary fitted strategies. This certainly explains their current popularity in the computational mechanics community for the analysis of geometrically complex objects (see [21, 22, 23, 24, 25, 26, 27, 28] to name a few). In the current study, we choose to resort to immersed isogeometric analysis [29, 30, 31, 32, 33] which provides a natural framework for performing fictitious domain analysis using smooth higher-order functions. After a first step devoted to the identification of a level-set based smooth boundary of the specimen that is imaged, we suggest constructing an automated immersed boundary DIB model using a regular high order B-spline grid in the same spirit as in [10]. The spline support will then be used as the discretization basis for image registration (same idea as in [34, 35, 36, 37] for instance). Returning to the area of DIB models, the contribution of our work is to adjust the modeling parameters (element size, polynomial degree, quadrature rule) so that the discretization error is comparable to that produced through the imaging (*i.e.*, pixelation) of the real specimen. The proposed study thus breaks with the usual practice in the field where the numerical convergence is most of time assessed with geometries deemed to be exact (such as in references [9, 10] for instance). This enables us to end up with a fairly-priced DIB model in the sense that going to a more refined model will not enable a better accuracy since the total error is dominated by the intrinsic geometry error coming from the image generation process.

Concerning now the experimental aspect, as previously indicated, kinematic measurements by DVC carried out during *in-situ* tests could constitute an interesting counterpart to the simulations. DVC consists in essence of finding the coefficients of a given kinematic basis that performs the best possible registration of the images recorded at rest and once the specimen loaded. DVC has been successfully applied to a wide range of natural and artificial materials [14, 38, 39, 40] presenting, once imaged, favorable textures at the macro-scale. The usual subset based approach [14] undertakes to solve a collection of independent image registration problems in sub-volumes (the so-called *subsets*) distributed in the Region Of Interest (ROI). In each subset, the displacement is usually assumed to be continuous and interpolated using low-order shape functions. Although widely used to study the targeted materials because of its simplicity and its computational efficiency, this approach may not appear relevant if the objective is to establish a dialog between the measurements and the results of mechanical simulations (in order to perform data assimilation for instance). As a result, a FE approach to DVC (often referred to as *global*) was later introduced by [41] to conveniently bridge the experimental and simulation outputs. In this variant, the images are registered by using a FE displacement field defined in the whole ROI. This approach provides access to globally continuous displacement fields, which can be naturally compared to the simulation results. A fine mesh would then be necessary to capture local kinematics when dealing with complex micro-structures, which would make the DVC problem ill conditioned since the kinematic basis becomes too rich with respect to the amount of (relevant) data provided by the imaging tool. However, this formulation of DVC can be easily regularized using Tikhonov like methods [42, 43, 44, 45] to compensate for a texture deficit under a given scale [46]. The idea is to add to the least-square correlation functional a regularization term introducing a new *a priori* on the displacement field [45]. This can consist in a "smoothness constraint" [44] or even a mechanical constraint [47, 48, 49, 46]. Recent contributions have for instance overcome the texture issue in trabecular bone samples [50] or wood cell materials [51] using regularization schemes based mostly on second-order Tikhonov operators. In this work, we consider a mechanically sound regularization similarly to [52]. From a global point of view, we seek here to exploit the information coming from the movement of cell boundaries (*i.e.*, the only significant gradients available) and rely on a mechanical model to estimate displacements in the textureless micro-structure, *e.g.*, in walls and/or struts. The question then becomes: how to automatically and efficiently construct a specimen-specific regularization term for the DVC to take into account the material architecture ?

In this context, it is appealing to get use of the previous image-based model and to use it both as a support for the measurement and to define a mechanical model that regularizes the DVC problem.

As a first application, we focus here on cellular materials such as open-cell or closed-cell foams. We next assume that they present only one characteristic structural scale, namely the cell scale. In addition,

the constitutive material is taken as isotropic at the micro scale. With this approximation, the material sample can be considered as a structure to which a mechanical model is applied. It is then possible to use this mechanical model in order to regularize the ill-posed DVC problem. Without loss of generality, the work presented here focuses only on two-dimensional cases. The proposed approach will then be illustrated using a 2D DIC algorithm and 2D images. Generalization to 3D, with expected difficulties both in terms of implementation and numerical complexity, will be addressed at a later stage. Lastly, rather than resorting to real images grabbed during an experiment, synthetic images are generated instead. A super resolved reference image I_r is created based on the CAD model of the cellular material. One can then get a super resolved image I_d in the deformed configuration by advecting I_r using the displacement field u of a pre-computed virtual test based on high resolution (boundary fitted) FE simulations. The resulting images and the computed displacement field used for their construction are next considered as ground truth data. They serve to challenge the DIB and DIC procedures. For instance, the images are downsampled at different resolutions in order to mimic the behaviour of the CCD sensor and evaluate the influence of the image resolution. They allow to simulate the whole chain: experiments, image sampling and quantization, noise, construction of a geometrical model, then a mechanical one (assigning properties according to gray-level information), and finally regularized measurement. Knowing the reference FE displacement field, one can then analyze the different sources of error (geometric error, numerical error, ultimate error of the DIC, etc.). From the general point of view of DIC, Fig. 1 illustrates the main ideas of our contribution. Given two images of the material captured during an *in situ* test, one in the reference state and the other once the sample has been loaded, we seek to identify the displacement field at a sub-cellular scale by DIC. To compensate for the poor texture, we suggest building an automated DIB model to regularize the ill posed DIC problem.

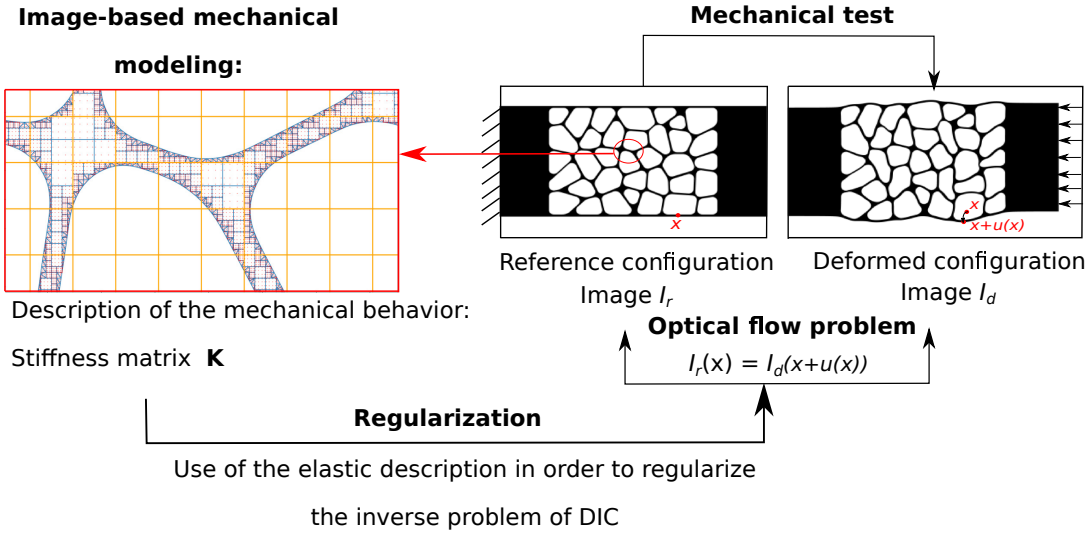

Figure 1: Synoptic view of the proposed approach to Digital Image Correlation (DIC) to perform displacement measurements in cellular materials below the cell scale. The images do not exhibit any texture under the cell scale and the DIC problem is therefore poorly conditioned below the cell scale. Similarly to [46], we propose here to use mechanical regularization to obtain sub-cellular displacement fields. In this work, a stiffness matrix that accounts for the underlying architecture is used. An immersed boundary approach is considered and fine-tuned to construct the latter. In this paper, the idea is to specify how to realize such a regularized measurement while mastering the associated cost.

The present paper is organized as follows: after this introduction, Section 2 is devoted to the construction of the fairly-priced immersed boundary DIB model. In particular, a careful numerical convergence analysis is conducted in order to properly adjust the numerical model parameters while taking into account the intrinsic geometry error coming from the image generation process. Then, in Section 3, the proposed DIB model is used to assist DIC in order to measure mechanically sound displacement fields at the sub-cellular scale. Finally, Section 4 concludes on this work by summarizing our most important points and motivating future research based on the proposed procedure.

2. A fairly priced image-based mechanical model

In this section, we present our strategy for generating a mechanical DIB model. We thereafter rely on a 2D cellular like material as shown in Fig. 1. Let us assume that we capture a representative digital image I_r of the sample, *i.e.*, in our case, that we record an undistorted fronto parallel picture. Such a digital image usually results from a relatively complex process, particularly in the case of tomography. However, the latter is generally composed of a set of regularly arranged pixels or voxels carrying information that may at first be related to a physical property (see step 1 of Fig. 2). The contrasts in the image plane are here assumed to result only from the underlying architecture. We consequently assume that the observed texture is binary and that it is simply quantized by the pixel.

The idea is to build, from the set of gray-levels data set grabbed in the ROI, a fairly priced mechanical model that accounts at best for the assumed local behavior of the real sample. Fig. 2 summarizes the different steps for the construction of a mechanical image-based model. In the context of this work, where only synthetic tests are performed, the images are generated by a simple algorithm that consists in assigning, for a given pixel region, a gray-value that represents the volume fraction and then quantizes it. We must emphasize that this procedure does not represent the sophisticated mechanism of real image acquisition and that other more realistic models exist, those including filling factors for instance [53]. Other external parameters such as noise can also induce non negligible errors. In this first study regarding the image-based model construction, the effect of noise is not examined for the sake of clarity. It will, however, be taken into account later on in Section 3 (see Section 3.2.4) that focuses on the application to DIC. In the following, we first present the process of constructing a geometric model from gray level data (see step 2 in Fig. 2). Based on this geometric model, we then construct an automated analysis model that approximates the elastic behavior of the image being observed (see step 3 in Fig. 2). Finally, a numerical convergence study is conducted in order to properly fix the parameters of the constructed mechanical model (element length, order of approximation and quadrature rule) such that the error obtained at step 3 of Fig. 2 is in the same order of magnitude as the one coming from the intrinsic geometry discrepancy produced through steps 1 and 2 of Fig. 2. In that sense, we will characterize our constructed image-based model (*i.e.*, including the correct parameter settings) as a fairly priced model. To the best of our knowledge, such a study has never been carried out in the field of image-based models. Indeed, the convergence of numerical methods in this context seems to be essentially investigated with geometries deemed to be exact (see, *e.g.*, references [9, 10]), and thus the existing unfitted image-based models certainly lead to over-calculations (too fine meshes and/or too high polynomial degrees).

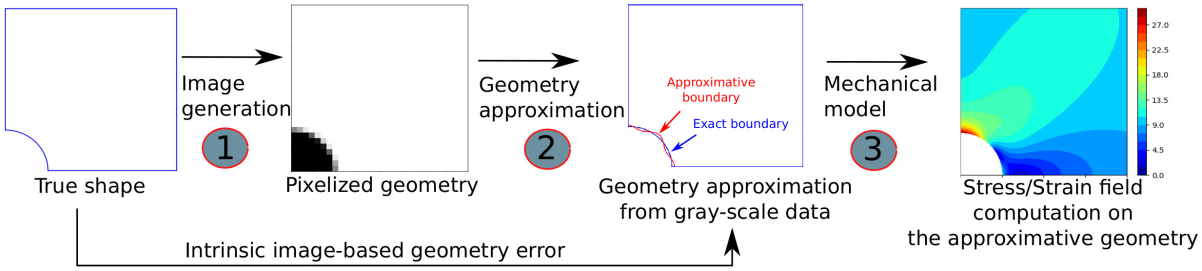

Figure 2: Summary of the different steps of the construction of a mechanical digital image-based model.

2.1. From gray-levels to geometric models

One of the main challenges in modeling complex materials with imaging is the segmentation of the different phases that constitute the material and their geometric representation. In the context of this work, a focus will be made on cellular-type materials (*i.e.*, with only one phase), therefore we will only use a binary geometrical representation which differentiates between void and material.

The description of the boundary can be classified into two main approaches: meshing methods and level-set methods. The meshing approach consists in thresholding the gray-scale data, then extracting a surface representation (using strategies such as the marching cubes algorithm [54, 18] for instance) and finally applying a meshing algorithm in order to produce a watertight finite element mesh (see Fig. 3c). Converting each preserved pixel into a linear finite element (see Fig. 3b) also allows to extract an implicit volume representation but presents geometric irregularities especially for low resolved images [2] in addition to a large computational cost. Generally, meshing methods need smoothing operations

before proceeding to the meshing step. The interested reader can also find other techniques based on the meshing of reconstructed surfaces from oriented point clouds [55]. Finally, it may be noted that recent works based on nested Cartesian grids (see, *e.g.*, [11]) allow to improve pure pixel models with hierarchical refinement, whose process is actually close from isogeometric refinement using hierarchical splines [29, 10]. Conversely, level-set methods consist of finding regular contours of elements directly

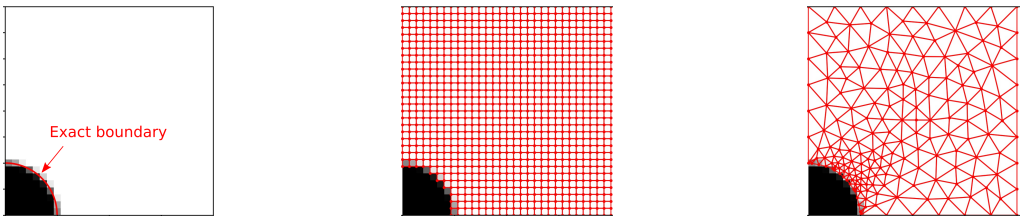

(a) Synthetic image of a rectangular plate with a quarter hole.

(b) Conversion of the binary image into a Q_4 finite element mesh.

(c) Finite element mesh resulting from the curve boundary obtained with the marching squares algorithm.

Figure 3: Conversion of an image into a finite element mesh.

within the initial images. A large class of level-sets named evolution level-sets propagate an initial curve using the convection-diffusion equation in order to fit the different regions in the image [56, 57, 58]. Another manner of identifying regular contours in images is to find a smooth physical representation with minimal oscillations and that conserves the local variations of the target images. A regular contour can therefore be obtained by taking an iso-value of the physical representation. This is the approach adopted in this work. We justify this choice because the obtained boundary is smooth and also by the fact that this geometry parametrization is mesh-free, which appears appealing in image registration (see Section 3 below). The Q_4 voxel based model and the marching squares algorithm will be used for comparison purposes only, as they can appear as the current practice in the field.

More precisely, our geometry description will be based on the smoothing B-spline surface [10] defined by (1)-(2)-(3). Let g be a piece-wise representation of an image of pixel size equal to Δx and Δy into the x and y directions, respectively. Using the *Cox–deBoor* formula [59], B-spline basis functions can be defined over the pixel domain denoted Ω. A general form for the smooth representation of the image g could be viewed as a linear combination of the B-spline basis functions:

$$\forall (x,y) \in \Omega \quad f(x,y) = \sum_{i=1}^{m} N_i^q(x,y) a_i, \tag{1}$$

where N_i^q is the set of m two-dimensional B-spline basis functions defined over open knot vectors of constant step size equal to pixel size Δx and Δy. The order q is practically chosen in $\{1,2,3\}$ depending on the image resolution and the degree of noise. A $\mathcal{C}^{q-1}$ regularity is applied on the interior knots. Using the isogeometric analysis formalism, the coefficients a_i are interpreted as the control points of the smoothing surface. In order to overcome the computational cost of a standard L^2 projection for fixing the coefficients a_i, it is possible to proceed as follows (see again [10]):

$$a_i = \frac{\displaystyle\int_\Omega g(x,y) N_i^q(x,y) dxdy}{\displaystyle\int_\Omega N_i^q(x,y) dxdy}. \tag{2}$$

Each coefficient a_i is the weighted average of the image over a region of a maximum of $(q+1)^2$ pixels due to the compact support property of B-spline functions. It can also be viewed as an L^2 lumped projection. The smoothing function obtained with the use of these coefficients has properties that make it suitable for extracting a smooth boundary by simply considering an iso-value equal to a threshold value. More precisely, the function is locally bounded by the minimum and maximum gray scale values. Furthermore, the authors in [10] have shown that this smoothing approximates a convolution with a Gaussian kernel. In the end, once the smoothing function is computed using (1)-(2), it is possible to characterize the boundary geometry by considering a threshold value g_t such as:

$$(x,y) \in \Omega_p \iff f(x,y) \geq g_t, \tag{3}$$

where Ω_p is the physical domain to be studied. Fig. 4 shows the obtained curve after thresholding the smooth representation of the image.

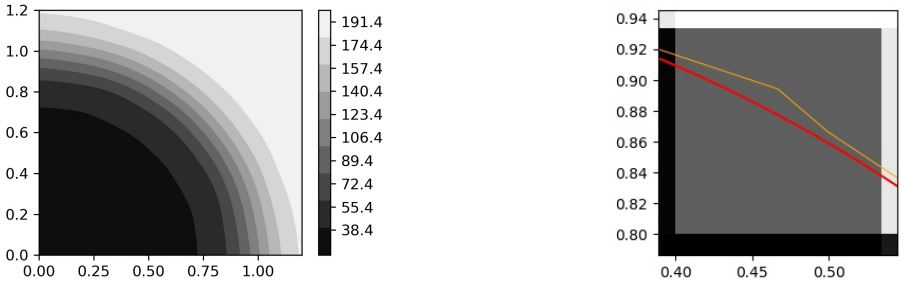

(a) Level sets of the cubic smoothing function defined in (1)-(2).

(b) Red: Iso-value of the cubic smoothing function using the level set defined in (1)-(2). Orange: marching squares boundary.

Figure 4: Extraction of a smooth boundary from an image of a one-phased sample.

2.2. From an image-based level-set geometry to mechanical analysis

Unlike the first class of methods (see, *e.g.*, Figs. 3b and 3c), the approach based on level-sets is not well suited for direct meshing since it only allows to obtain a spatial interrogation function of any physical point. With this representation, unfitted boundary meshing techniques such as the Finite Cell Method (FCM) [21], the Cut-FEM method [24] or the Extended Finite-Element Method (X-FEM) [60, 5] are more appropriate. The use of the X-FEM for building image-based models was suggested in [5, 6, 7] and was applied to two phases materials such as those which present inclusions. Roughly speaking, all these methods have the same purpose which is to accurately integrate discontinuous functions. We choose to adopt here the B-spline FCM due to its computational simplicity related to the tensor product nature of B-spline basis functions and its high regularity. That is also interesting for the regularization of image registration [36, 61] (see Section 3 below). The B-spline FCM consists in embedding the domain of analysis in a simple rectangular domain and transferring the geometrical representation from the mesh to the integration scheme. In this case, the only role played by the mesh is the generation of a set of functions suited for analysis. It has been successfully used for image-based analysis for, *e.g.* a metal foam specimen [30] and a trabecular bone specimen [10]. In the following, we briefly recall this method and present our implementation to build our image-based model. In particular, we make use of most of the treatments suggested in [10].

As in (3), we refer to Ω_p as the physical domain known by a level-set function. After embedding this domain in a rectangle, the complementary of Ω_p is called the fictitious domain and is denoted Ω_f. In linear elasticity, with the absence of volume forces, the fictitious domain method consists in solving the principle of virtual work with a penalization of the stress tensor σ. The constitutive behavior law is modified by considering the penalized stress tensor [30] defined by:

$$\sigma_\alpha(x,y) = \alpha(x,y)\sigma, \tag{4}$$

with

$$\alpha(x,y) = \begin{cases} \alpha_p = 1 \quad \forall (x,y) \in \Omega_p \\ \alpha_f = 10^{-n} << 1 \quad \forall (x,y) \in \Omega_f \end{cases} . \tag{5}$$

The Finite Cell Method consists in solving the variational problem using a classical Galerkin approach on a structured grid with high-order basis functions. The elasticity problem is therefore reduced to a linear system $\mathbf{Ku} = \mathbf{f}$ where $\mathbf{u}$ is the vector of displacements at the control points of the embedding B-spline grid (defined on $\Omega = \Omega_p \cup \Omega_f$), $\mathbf{f}$ is the force vector and $\mathbf{K}$ is the stiffness matrix. The integration of the penalized term coming from (4)-(5) with the standard Gauss quadrature is no longer valid in a cut element due to the discontinuity introduced. Knowing the parametrization of the boundary of the physical domain, a geometrical approximation can be performed using a quad-tree decomposition. Each element of the structured mesh (called a cell in the FCM terminology) is divided into four sub-cells if it cuts the boundary (see Fig. 5a). The sub-cells that do not cut the geometric boundary are integrated with a full Gauss quadrature. This decomposition is repeated until a predefined maximum

level is reached. Of course, the larger the number of quad-tree levels the higher the accuracy of the Finite Cell Method. This induces a large number of integration points which increases the numerical cost of the method. In order to tackle this problem, multiple recent methods were developed for the integration of cut cells (such as linear tessellation strategies [10], smart boundary conforming octrees [62] and moment fitting methods [63, 64, 65]).

In this work, for simplicity and robustness, we make the choices below for building the fictitious domain-type stiffness matrix $\mathbf{K}$. We remind here that the objective of next section will be to properly fix the parameters of this simple scheme to allow for the construction of a fairly priced mechanical model.

- Linearization of the boundary for the integration on the physical domain: when using the smooth physical representation (1)-(2)-(3), we perform a linearization of the geometric boundary [10] (see Fig. 5c). At a certain level of decomposition, a cut sub-cell is detected by an interrogation of sampled points uniformly distributed along its boundary. If at least one point has a value greater than the threshold value, in the opposite of the other points, the sub-cell intersects the material interface and the quad-tree algorithm subdivides it into four new sub-cells. In the contrary, if the level-set function has values greater or smaller than the threshold value on all sampling points, the sub-cell is homogeneous and it is subsequently integrated with a full Gauss quadrature. For the last cut sub-cell, the boundary intersection with each sub-cell side is approximated by considering the iso-value of the linearized level-set function at the sub-cell vertices (see again [10] for more details). The intersection points including the cell boundary vertices define a convex hull that is then given to a triangulation routine such as the Delaunay algorithm [66]. An exact quadrature rule is subsequently used for the integration of the closure simplices (see Fig. 5c).

- Fictitious domain integration: Using the additivity of the integral, the integration of the penalized term is obtained using the following equality:

$$\int_{\Omega} \alpha r dx dy = \int_{\Omega_p} (\alpha_p - \alpha_f) r dx dy + \int_{\Omega_p \cup \Omega_f} \alpha_f r dx dy, \tag{6}$$

  where r is a function defined on Ω. The final stiffness matrix is therefore given by:

$$\mathbf{K} = \mathbf{K}_{\Omega}(\alpha_f) + \mathbf{K}_{\Omega_p}(\alpha_p - \alpha_f). \tag{7}$$

  With this approach, $\mathbf{K}_{\Omega}$ is assembled with a standard Gauss integration scheme (see Fig. 5b) and $\mathbf{K}_{\Omega_p}$ is assembled with a quad-tree complemented by a tessellation scheme (see Fig. 5a). Such a treatment allows to save some integration points and thus some computational time in contrast to the more rudimentary approach consisting in performing $\mathbf{K}_{\Omega_f}(\alpha_f) + \mathbf{K}_{\Omega_p}(\alpha_p)$. Indeed, the immersed boundary is addressed here for only one cut domain (only Ω_p and not Ω_f, see [30] for more information).

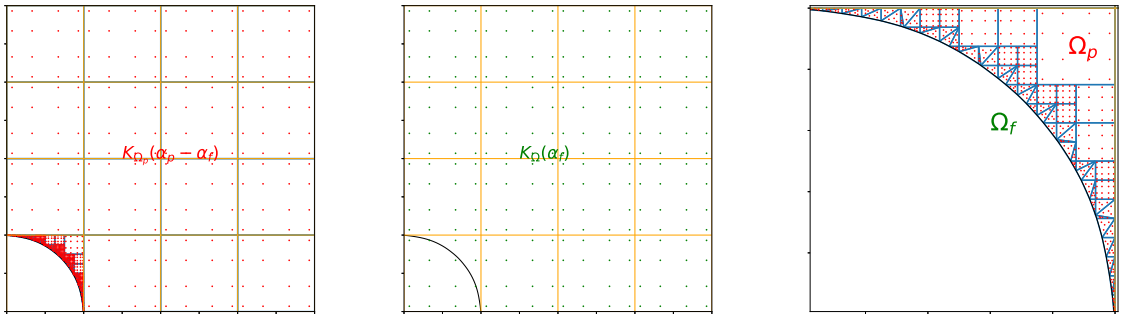

(a) Integration only on the physical domain with a penalization equal to $\alpha_p - \alpha_f$.

(b) Integration on the total domain with a penalization equal to α_f.

(c) Integration of a cut element. Zoom on the cut element of Fig. 5a. Red points are the Gauss integration points.

Figure 5: Quad-tree scheme for the integration of elements. The orange grid represents the embedding B-spline space.

For even more computational efficiency and for conditioning improvement, the fictitious degrees of freedom, which are associated to the basis functions that have a complete support lying in the fictitious domain could be removed because they do not influence the solution in the physical domain. In this work, we keep all the basis functions as they are integrated with the penalization factor α_f (see again Eq. (5)) and solve the linear stiffness system using a direct solver. We will see in Section 3 that such a treatment also simplifies the implementation of the regularization scheme for performing image registration. In all the following numerical tests, we consider a penalization factor $\alpha_f = 10^{-8}$. Regarding the convergence of such FCM schemes, it has been shown (*e.g.* in [67]) that they meet the same convergence properties as the standard boundary fitted methods.

Remark 1 (Boundary conditions)**.** *In this work, Dirichlet boundary conditions are imposed only on complete (exterior) horizontal or vertical boundaries. In this simple case, Dirichlet boundary conditions are directly imposed on the degrees of freedom of a whole side of the embedding domain. In more general situations, let us notice that Dirichlet boundary conditions can no longer be directly applied and weak boundary condition strategies are used [68, 30].*

2.3. Analysis of the geometry error and its propagation in the mechanical solution

We now truly apply the B-spline variant of the Finite Cell Method to synthetic images using the level-set function defined in (1)-(2)-(3). We start by conducting a geometry convergence study in order to fix the sufficient number of quad-tree levels that should be chosen practically and then present a numerical investigation of the immersed boundary method applied to level-set images in order to set the other discretization parameters (mesh size h and polynomial degree p). We recall that our objective is to end up with a fairly-priced mechanical model in the sense that going to a more refined model will not offer better accuracy since the total error will become dominated by the intrinsic geometry error coming from the image generation process.

2.3.1. Numerical investigation of the level-set geometry error

To start with, we consider a very simple, one-dimensional example. More precisely, we undertake to compute the length of the support of a step function represented by a one-dimensional image. Given an analytical step function V defined by:

$$V(x) = \begin{cases} v_{max} & x \in [0, c[\\ v_{min} & x \in]c, l] \end{cases} \qquad \text{with} \quad v_{max} > v_{min} \quad \text{and} \quad c < l, \tag{8}$$

we assume that we have acquired a one-dimensional image defined by a set of pixels $(g_i)_{i \in [\![0,n]\!]}$ and that represents a sampled version of V (see Fig. 6, left and middle). We construct an image by assigning a maximum gray-level value denoted v_{max} to all the pixels that are completely in the domain $[0, c[$ and a minimum value denoted v_{min} to those in the domain $]c, l]$. The pixel that cuts the discontinuity of the step function is assigned with a mean gray-level value weighted by the intersection lengths. Fig. 6 (middle and right) shows the procedure that consists in constructing the smooth representation of the image.

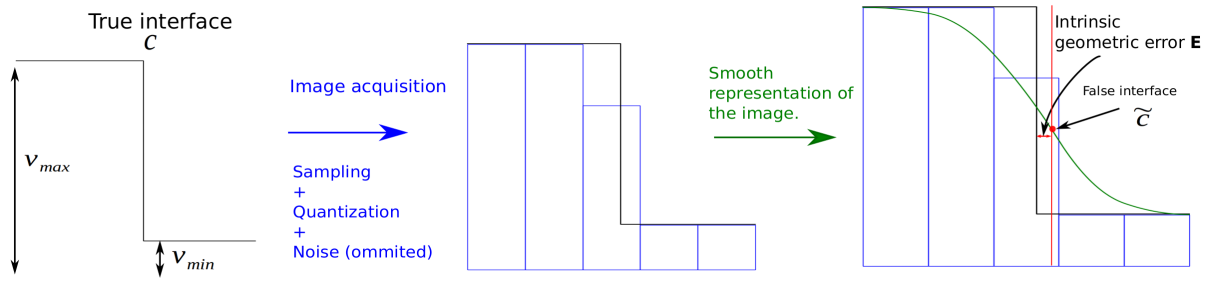

Figure 6: Steps for constructing the synthetic image and the use of a smooth representation of the image.

Starting from a one-dimensional mesh, we apply the one-dimensional version of the quad-tree scheme of Fig. 5c in order to estimate the value of the true interface c. We denote this quad-tree approximation of the interface c_a. In addition, we denote $\tilde{c}$ the abscissa of the threshold value of the smoothing function (see Fig. 6 right). As (1) cannot be inverted directly, $\tilde{c}$ is found using a Newton-Raphson algorithm

in a small neighborhood near the interface. The geometric approximation of the interface induces that $c \neq \tilde{c} \neq c_a$ (see Fig. 7). We introduce the three errors listed below:

- Intrinsic geometry error:
$$E = \left| \frac{c - \tilde{c}}{c} \right|, \tag{9}$$
it represents the difference between the true interface and the exact value of the "false" interface.

- Total geometry error:
$$\bar{E} = \left| \frac{c_a - c}{c} \right|, \tag{10}$$
it represents the difference between the estimation of the false interface (using the one-dimensional quad-tree scheme) and the true interface.

- Domain integration error:
$$\tilde{E} = \left| \frac{c_a - \tilde{c}}{\tilde{c}} \right|, \tag{11}$$
it represents the quad-tree integration error with respect to the false geometry. More precisely, this error comes from the linearization of the interface in the last sub-cell. In other words, it measures how we accurately integrate the false geometry.

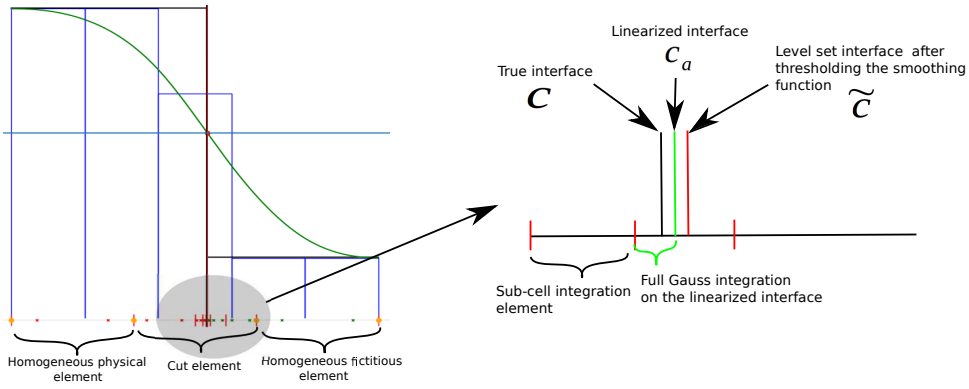

Figure 7: The different interfaces of the geometry approximation.

The position of the interface c within one pixel influences the accuracy of the geometry approximation. Fig. 8 shows that the acquisition process induces an error when the pixel does not intersect the interface symmetrically. The error is minimal when the interface is located exactly at the center or at the boundaries of a pixel. The maximum error is about 5×10^{-2} pixels (*i.e.* a 2% relative error).

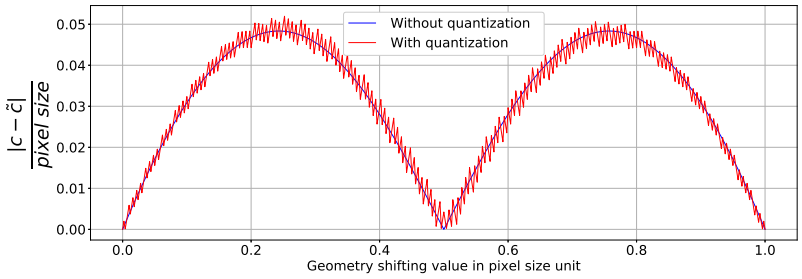

Figure 8: Evolution of the intrinsic geometry error in pixel size unit when translating the true geometric interface all over one pixel.

Another important user-defined parameter for estimating the interface is the threshold value. A pragmatic choice is adopted here: we set this value denoted g_t (see Eq. (3)) to the mean gray value:

$$g_t = \frac{v_{min} + v_{max}}{2}. \tag{12}$$

The threshold g_t is dependent of the chosen level-set method (*i.e.* the manner how the physical representation of the image is constructed) and the image resolution. The determination of the threshold criteria is still a practical open question. We believe that experimental calibration strategies could help adjusting the threshold criteria with respect to physical properties of the imaged specimen. The interface c_a is calculated by summing the lengths of the integration sub-cells. We recall that we perform a linearization of the level-set at the finest level (one-dimensional version of the tessellation shown in Fig. 5c). Denoting x_{min} and x_{max} the extremities of the last sub-cell and f_{min} and f_{max} the evaluation of the smoothing function at x_{min} and x_{max} respectively, the linear approximation of the interface denoted c_a can actually be computed as:

$$c_a = \frac{g_t - b}{a}, \quad \text{with} \quad a = \frac{f_{max} - f_{min}}{x_{max} - x_{min}} \quad \text{and} \quad b = \frac{f_{min}x_{max} - f_{max}x_{min}}{x_{max} - x_{min}}. \tag{13}$$

In order to fix the sufficient sub-cell level, we conduct a convergence study using the different errors $E, \bar{E}$ and $\tilde{E}$ defined in (9), (10) and (11), respectively. We vary the quad-tree algorithm's maximum level. Due to the influence of the location of the boundary interface as shown in Fig. 8, each error considered is computed for the worst acquisition configuration, *i.e.*, the configuration in which the geometry error is maximum (see Fig. 8 again). Fig. 9 shows the evolution of the two errors $\bar{E}$ and $\tilde{E}$ for two image resolutions. The corresponding intrinsic geometry error E is also put on this figure. We observe that the error $\bar{E}$ converges to the intrinsic geometry error E and that the image resolution improves the geometry approximation (the intrinsic geometry error is reduced from left to right). The integration error $\tilde{E}$ goes down to zero and intersects the geometry error E for a sub-cell size equal to the pixel size. This induces that there is no interest for refining the domain of integration beyond the size of a pixel since the intrinsic geometry error is already achieved. In other words, going to higher quad-tree integration levels would necessary lead to over-calculations.

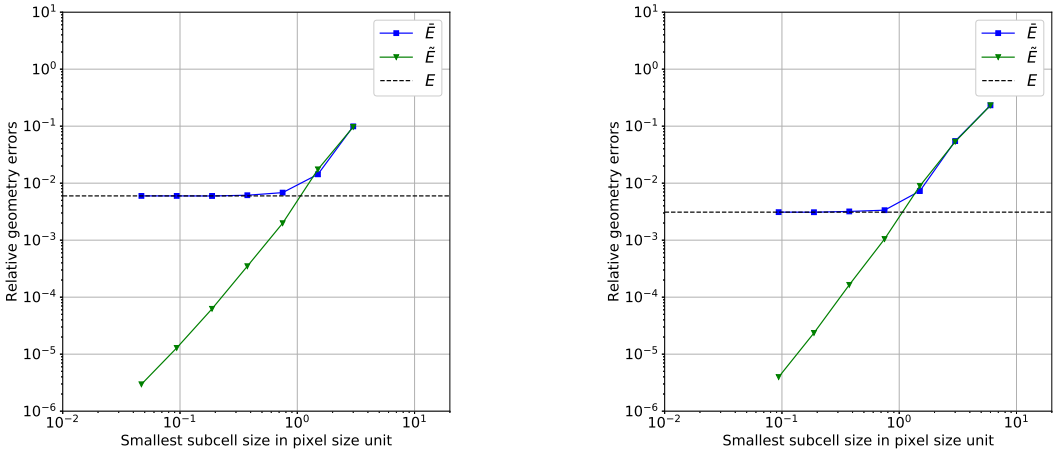

(a) 6 pixels in the image.

(b) 12 pixels in the image.

Figure 9: Intrinsic geometry error E displayed along with the evolution of the errors $\bar{E}$ and $\tilde{E}$ with respect to the size of the smallest sub-cell in pixel size units (1D test case).

We then reproduce the previous numerical experiment for a two-dimensional case by considering the geometry depicted in Fig. 3a. The image is generated with a gray-level filling algorithm based on volume fraction similar to the one used in the 1D example related to Eq. 8. The pixels that are respectively inside and outside the circle's boundary are assigned with a minimum gray-level value v_{min} and a maximum gray-level value v_{max}. The pixels that intersect the circle's boundary are assigned with a mean gray-level value. Using the level-set method, we approximate the circle boundary by setting again a threshold value defined by (12). In order to quantify the geometry error, we detect a large number of radii spanning $\theta_{min} = 0$ to $\theta_{max} = \pi/2$ of the smoothing function by applying a Newton-Raphson algorithm on the radial axis. The exact geometry for Fig. 3a is defined for the exact radius $R = 1$ and a length of the plate equal to $L = 4$.

We investigate the convergence of the quad-tree algorithm by considering the approximation of the area of the plate. Similarly to the one-dimensional study, we define the following errors, *i.e.* the intrinsic

geometry error E, the total geometry error $\bar{E}$ and the domain integration error $\tilde{E}$ such that:

$$E = \frac{|\tilde{A} - A\,|}{A}, \quad \bar{E} = \frac{|A_a - A|}{A} \quad \tilde{E} = \frac{|A_a - \tilde{A}|}{\tilde{A}}. \tag{14}$$

A_a is the approximation of the area bounded by the level-set. It is equal to the sum of areas of the integration sub-cells. $\tilde{A}$ is the area of the level-set geometry defined by:

$$\tilde{A} = L^2 - \int_{\theta=\theta_{min}}^{\theta=\theta_{max}} \int_{r=0}^{r=\mathcal{R}(\theta)} r dr d\theta, \tag{15}$$

where $\mathcal{R}(\theta)$ is the radius of the level-set approximated circle, which depends on the angle θ. $\tilde{A}$ can be numerically computed by:

$$\tilde{A} = L^2 - \frac{\theta_{max} - \theta_{min}}{2n_\theta} \sum_{i=1}^{n_\theta} \mathcal{R}_i^2, \tag{16}$$

where each $\mathcal{R}_i$ is the radius abscissa, *i.e.* such that the smoothing function is equal to the threshold iso-value, and n_θ is the number of angles considered (here $n_\theta = 10^6$). A is the exact area of the plate defined by:

$$A = L^2 - \frac{(\theta_{max} - \theta_{min})R^2}{2}. \tag{17}$$

In Fig. 10, we plot the evolution of the errors E, $\bar{E}$ and $\tilde{E}$ with respect to the size of the smallest integration sub-cell, similarly as in Fig. 9. We perform the numerical test for two different image resolutions. We obtain the same behavior as in the one-dimensional case. As a consequence, a sufficient quad-tree level can be chosen so that the smallest integration element has approximately a size equal to the pixel size. Let (n_x, n_y) be the number of pixels of an image and (n_x^e, n_y^e) the number of elements of the B-spline embedding mesh. From a practical view point, the sufficient quad-tree level for an accurate estimation of the area can thus be chosen using the following formula:

$$l = \left\lceil \frac{1}{2} \log_2 \left(\frac{n_x n_y}{n_x^e n_y^e} \right) \right\rceil, \tag{18}$$

where $\lceil \bullet \rceil$ denotes the ceiling function. In the rest of this work, the number of integration sub-cells will be fixed by the constant defined in (18).

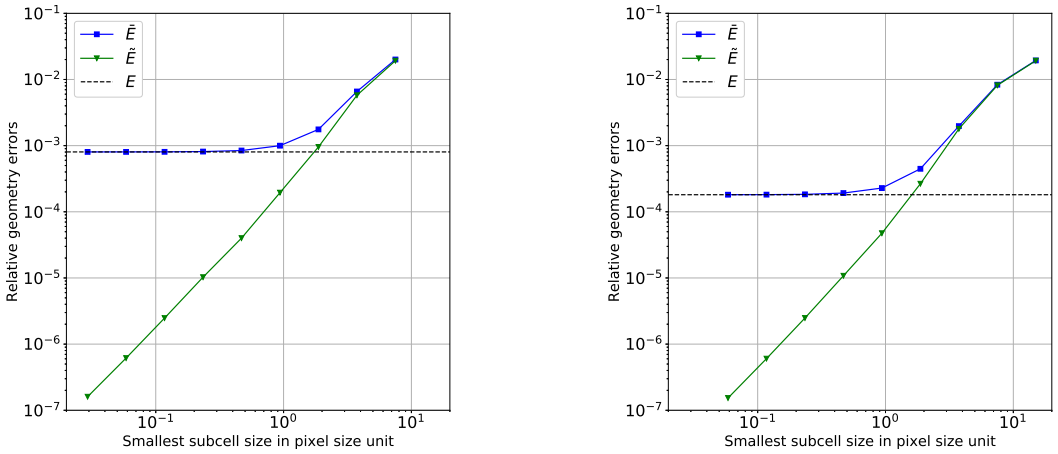

(a) 30×30 pixels in the image.

(b) 60×60 pixels in the image.

Figure 10: Intrinsic geometry error E displayed along with the evolution of the errors $\bar{E}$ and $\tilde{E}$ with respect to the size of the smallest sub-cell in pixel size units (2D open-hole plate test case).

In order to study local curvatures influence, the same analysis was undertaken on more complex geometries. For instance, polar curves defined by $\mathrm{R}(\theta) = R + 0.1\sin(\omega\theta)$ were considered (inspired from [69]). For the tests performed with $\omega = 8$ and $\omega = 16$, a similar error evolution as the one shown in Fig.10 was obtained.

2.3.2. Numerical convergence of the image-based model: adjustment of the last discretization parameters

After identifying the sufficient number of quad-tree levels, we study in this section the numerical convergence of the mechanical solution of the image-based level-set geometry. For this purpose, we start by considering the same geometry as the one presented in Fig. 3a to which we now add the boundary conditions depicted in Fig. 11. This test case is equivalent to solving an infinite open-hole plate in tension. We fix the material properties as follows: $E = 10^5 Pa$ and $\nu = 0.3$, where E is the Young's modulus and ν is the Poisson ratio. When considering a far-field traction denoted T_x that we fix to $10Pa$, the stress field can be expressed in an analytical form (see, *e.g.*, [70] for the formula). This one is applied at the top and right boundaries.

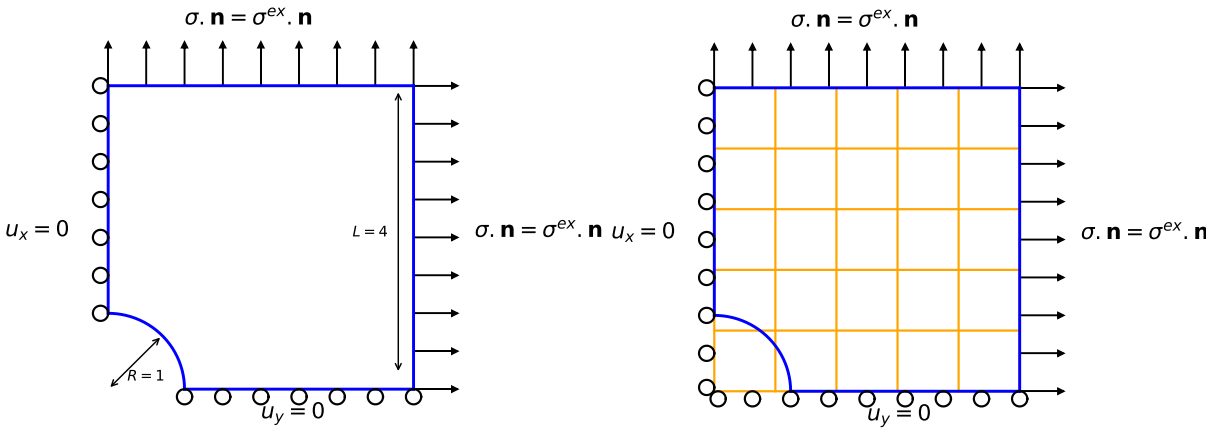

(a) Mechanical problem definition.

(b) An example of the embedding B-spline elements with the corresponding boundary conditions.

Figure 11: Mechanical problem definition: elastic plate with a quarter hole.

In the following, we investigate the convergence of the image-based immersed boundary model defined previously under mesh refinement and confront it to three other reference FE image-based models listed below:

- Q_4 **voxel-based model**: Threshold of the initial image and conversion of the pixel connectivity into Q_4 finite elements after a binary segmentation [2] (see Fig. 3b).
- **Marching squares without smoothing**: Contour detection using the linear Marching squares algorithm (two-dimensional version of the marching cubes algorithm [54, 71]) and meshing of the closed curve boundary (see Fig. 3c).
- **Mechanical properties based on gray-levels**: Converts each image pixel to a Q_4 finite element which has an elastic behavior based on the pixel's gray-level value. More precisely, the model's Young's modulus (denoted here Y) can be defined as a linear function of gray-levels:

$$Y(v) = \frac{v - v_{min}}{v_{max} - v_{min}} E_{max} + \frac{v_{max} - v}{v_{max} - v_{min}} E_{min} \tag{19}$$

  where v is the element's gray-level value, $E_{max} = E$ and $E_{min} = \alpha E$ with α a penalization parameter equal to $\alpha_f = 10^{-8}$. This method has always a number of elements equal to the number of pixels and therefore induces a large number of degrees of freedoms. However, it has a particular interest when dealing with heterogeneous materials that have different material properties [12].

Based on the exact solution defined over the exact domain Ω^{ex}, we consider the error in energy norm defined as:

$$E^h = \sqrt{\frac{\int_{\Omega^{ex}} (\sigma^{ex} - \sigma^h) : (\varepsilon^{ex} - \varepsilon^h) dx}{\int_{\Omega^{ex}} \sigma^{ex} : \varepsilon^{ex} dx}}, \tag{20}$$

where ex and h subscripts stand for, respectively, the exact and the image-based solutions for each of the methods listed above. $A : B$ is defined by $A : B = tr(AB)$, where tr is the trace of a square matrix.

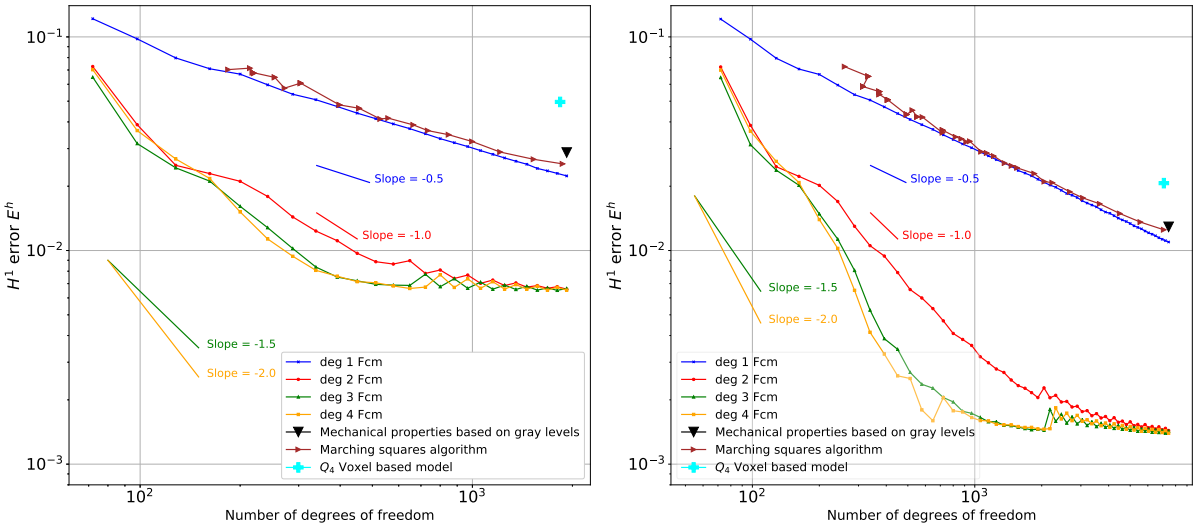

(a) 30 × 30 pixels in the image.

(b) 60 × 60 pixels in the image.

Figure 12: Evolution of the error in energy norm under mesh refinement for the elastic plate with a quarter hole.

Fig. 12 shows the results obtained in terms of convergence under mesh refinement for two image resolutions. More precisely, "deg 1 Fcm", "deg 2 Fcm", "deg 3 Fcm" and "deg 4 Fcm" denote the solution of the proposed image-based immersed boundary model when considering the quad-tree level of Eq. (18) and for polynomial degree $p = 1$, $p = 2$, $p = 3$ and $p = 4$, respectively. We observe that the theoretical convergence rate is obtained. The convergence is of order $O(h^p) \approx O(ndof)^{-p/2}$, where $ndof$ is the number of degrees of freedom and h is the equivalent size of the element. However, the high order solutions converge to an asymptotic value. This result is totally novel and breaks with what is more usually encountered in the field where the convergence of numerical methods is most of time assessed from resulting geometries deemed to be exact (*e.g.*, see [9, 10] again). Here, since we take into account the additional error due to the pixelation of the image (see step 1 in Fig. 2), we are able to observe an asymptotic constant behavior which means that there is no need to go to too fine models for optimal accuracy. Indeed, after a certain refinement level, the total error becomes dominated by the intrinsic geometry error coming from the initial image generation process. Last but not least, Fig. 12 shows that the proposed image-based model is significantly more accurate (for a given number of degrees of freedom) than the three voxel-based methods represented by the triangular dots and the cross dot. In fact, the cubic variant of the proposed model allows to gain approximately one order on the computational cost and precision. This accounts for the use of an advanced image-based, higher-order, fictitious domain type model in comparison to more standard voxel-based methods even when taking into account the intrinsic geometry error inherent to the image generation process.

More precisely, we will consider $p = 3$ for our model since it seems that we do not increase the accuracy with higher orders. This appears in contrast with what is usually advised in the current literature, which is, once again, due to the fact that we take into account the pixelation error in the process here. Regarding the size of the element, the idea would be to take the one corresponding to the beginning of the stagnation of the error. It depends on the test case. However, we will see in Section 3 that for cellular materials we can consider a size of element such that it encompasses the thickness of a fiber to correctly reproduce local bending. For completeness, Fig. 13 shows the evolution of the error as a function of the number of quadrature points for the mesh refinement range used in Fig. 12. More precisely, the proposed unfitted models with $p = 2$ and $p = 3$ are studied along with the two standard voxel-based approaches, *i.e.* the Q_4 voxel-based model and the model where the mechanical properties are affected from the gray-levels. Since the chosen quad-tree level is such that the minimal sub-cell size is not lower than the pixel size, we can observe the same global behavior as for the degrees of freedom in Fig. 12; that is, for a given number of integration points, our unfitted image-based model is significantly more accurate than the voxel-based methods. This confirms the fairly-priced property of our model.

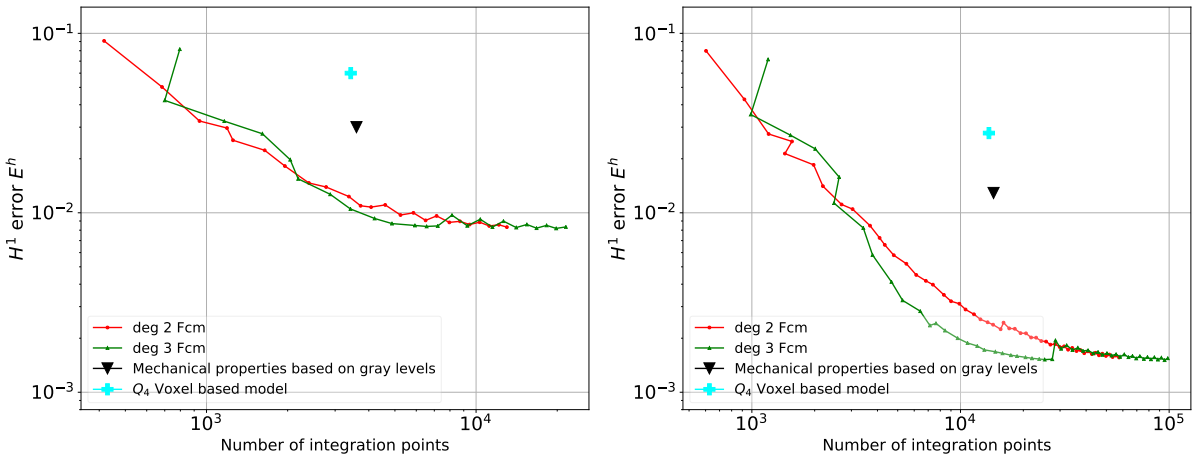

(a) 30×30 pixels in the image.

(b) 60×60 pixels in the image.

Figure 13: Evolution of the error in energy norm with respect to the number of integration points.

Remark 2. *At this stage, we should note that such results depend on the volume fraction of the cellular material since the number of degrees-of-freedom as well as the number of integration points for the standard voxel-based strategies decrease with the diminution of the volume fraction. In other words, when having a micro-structure with more holes than in the geometry of Fig. 11, the voxel-based strategies may behave better than in Figs. 12 and 13. This would even be more pronounced if one makes use of,* e.g., *nested FE meshes methods [11] that can be viewed as improvements of standard voxel-based approaches. However, let us note that some local mesh refinement techniques could also be used in the context of immersed isogeometric methods to decrease the number of degrees-of-freedom and of integration points in the void parts (see,* e.g., *[29, 10] that call upon of hierarchical B-spline functions).*

In order to come closer to real cellular micro-structures, we consider a second numerical example, for which we compare the different solutions visually. We investigate the mechanical problem defined in Fig. 14a where the geometry is subjected to the displacement load $u_0 = -1$. The center point of the hexagonal geometry is $(0, 0)$ and the other inclusion centers are the vertices of the hexagon centered at $(0, 0)$ and of length equal to $L = 50$. The inclusion radius is equal to $R = 22$. We set the material's properties to $E = 73.1 \times 10^9 Pa$ and $\nu = 0.33$. Fig. 14a displays the finite element mesh of the exact geometry on the underlying constructed image while Fig. 14b shows the B-spline embedding mesh.

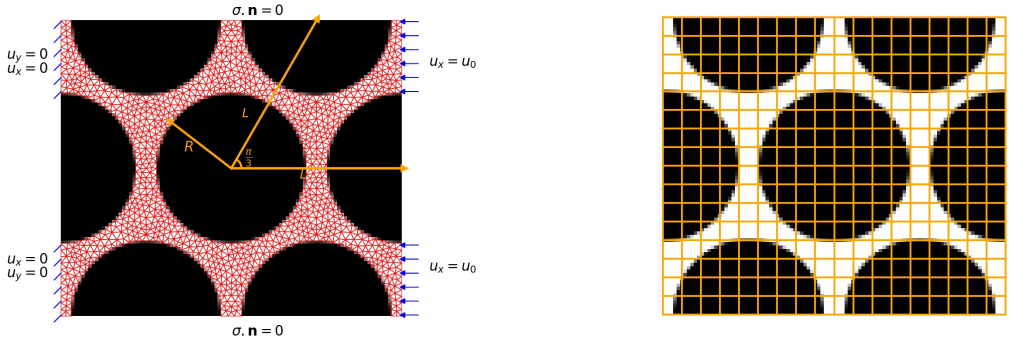

(a) Mechanical problem defined on a simplified micro-structure displayed with a linear finite element mesh of the exact geometry.

(b) Embedding B-spline mesh.

Figure 14: Mechanical problem: micro-structure with a hexagonal structure

We visualize in Figs. 15 to 18 the Frobenius norm of the strain tensor which can be viewed as an equivalent Von Mises strain field:

$$\varepsilon_{vm} = ||\varepsilon||_F = \sqrt{tr(\varepsilon^T \varepsilon)} = \sqrt{\varepsilon_{xx}^2 + \varepsilon_{yy}^2 + 2\varepsilon_{xy}^2}. \tag{21}$$

We compare the strain norm for the different methods in Fig.12. In addition, we put on the right of each figure the reference solution coming from a boundary fitted mesh that is more refined than the one depicted in Fig. 14a. Obviously, the strain field obtained using the proposed model has the highest smoothness compared to the other alternatives. We observe that the marching squares and the voxel based models allow to obtain similar strain fields but with more roughness. Finally, Tab. 1 indicates the number of degrees-of-freedom considered for each model. We emphasize that, in contrast to voxel-based approaches that are constrained by the image resolution, the immersed approach has the advantage of uncoupling the discretization of the solution space from that of the geometry, and therefore allows to keep the same B-spline approximation space for different image resolutions.

	Cubic Finite Cell Method (Fig. 15)	Marching squares algorithm (Fig. 16)	Q_4 voxel based model (Fig. 17)	Gray-level properties (Fig. 18)
50×43 pixels	798	3276	1728	4488
100×86 pixels	798	16432	5916	17574

Table 1: Comparison of the number of degrees of freedom for each image-based model (hexagonal micro-structure problem).

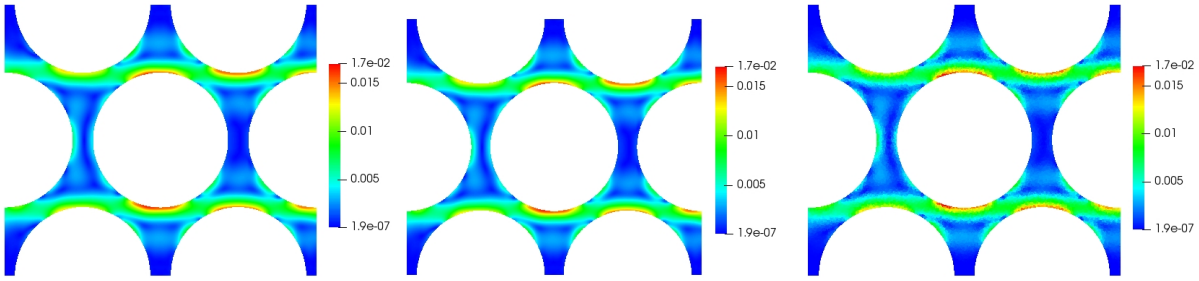

(a) 50×43 pixels. (b) 100×86 pixels. (c) Refined finite element solution.

Figure 15: Finite Cell Method using the level-set geometric representation. Cubic B-spline mesh corresponding to Fig. 14b.

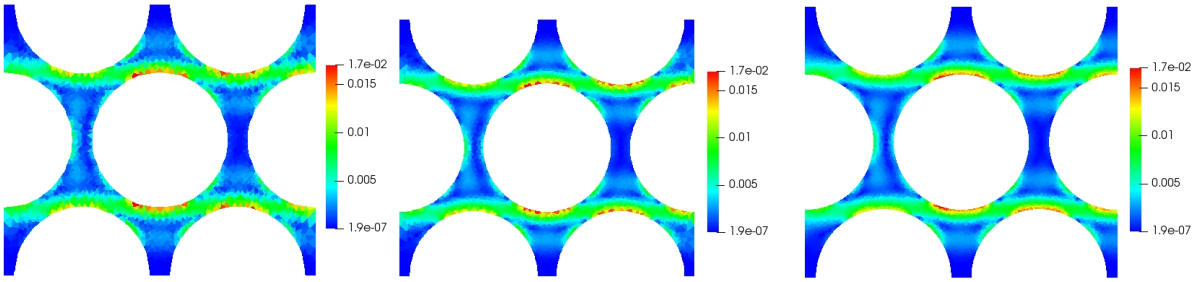

(a) 50×43 pixels. (b) 100×86 pixels. (c) Refined finite element solution.

Figure 16: Marching squares algorithm solution.

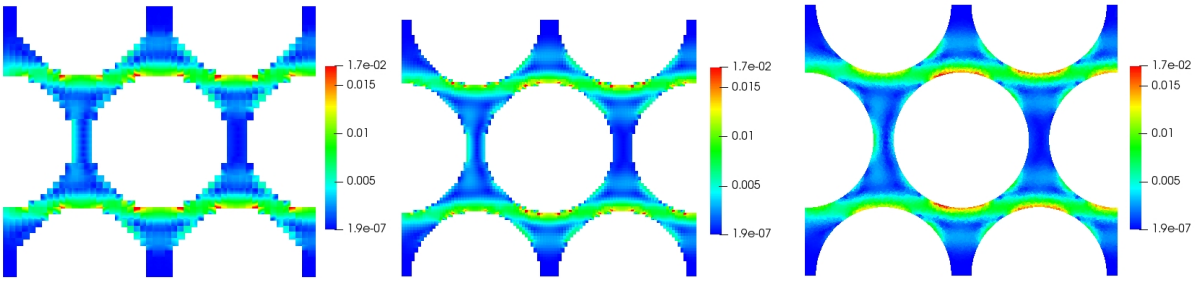

(a) 50 × 43 pixels. (b) 100 × 86 pixels. (c) Refined finite element solution.

Figure 17: Q_4 voxel based model

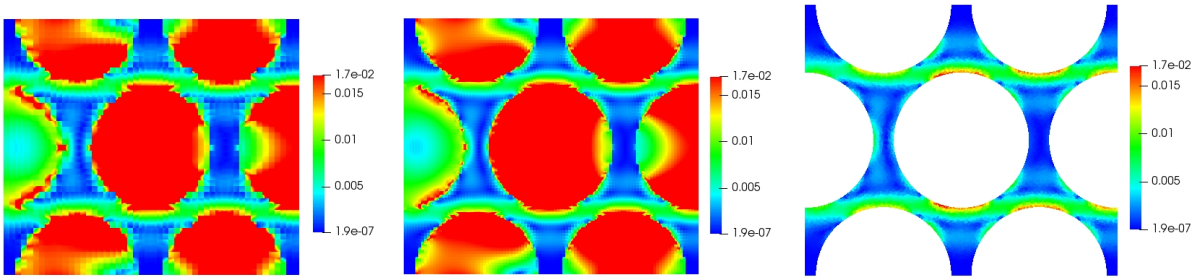

(a) 50 × 43 pixels. (b) 100 × 86 pixels. (c) Refined finite element solution.

Figure 18: Mechanical properties based on gray-levels. Post-processed stress field on the complete mesh.

3. Specimen-specific regularization of digital image correlation

Let us now consider a pair of digital images before and after a virtual mechanical test on a cellular specimen. We try, in this section, to identify the displacement and strain fields using Digital Image Correlation. As mentioned in the introduction, DIC is an inverse problem which is particularly ill-posed when focusing at the sub-cellular scale. The DIC algorithm used herein relies on a global interpolation of the unknown displacement field using the same cubic B-spline functions. This Galerkin approach naturally introduces a first kind of spatial regularization. Roughly speaking, the larger the size of the B-spline grid elements the higher the regularization of the optimization problem. This regularization allows to capture large disparities such as translations and rotations. However, when dealing with complex micro-structures such as cellular materials, local strains are expected, which cannot be described using an interpolation-based regularization with a coarse grid. Consequently, we need to reduce the impact of the interpolation-based regularization by refining the embedding mesh and to add a more softly regularization scheme in order to suppress non-physical local solutions. For that, most common algorithms consider the Tikhonov regularization term which consists in smoothing the displacement field by either penalizing the gradient norms or the curvature given by the norm of the Hessians of the displacement components. Based on the same principle, another, more mechanically-sound, alternative exists especially in the field of structural experimental mechanics: it can be referred to as an elastic regularization.

The image-based mechanical model built from the reference image is assumed to accurately describe the elastic behavior of the observed region. We thus propose to use this specific model to regularize DIC in the aim of estimating local strains fields within cellular materials.

3.1. Digital Image Correlation: brief overview and a focus on elastic regularization

DIC is a general computational method for finding spatial transformations between different image configurations. Given two gray-scale images I_r and I_d representing the reference and the deformed configuration of a material sample, DIC can formally be expressed as the following optimization problem:

$$\underset{u\in[L^2(\Omega)]^2}{\arg\min}\ \left[\mathcal{S}(u, I_r, I_d) + \lambda\mathcal{R}(u)\right], \tag{22}$$

where $u : \Omega \subset \mathbb{R}^2 \to \mathbb{R}^2$ is the unknown displacement field and Ω is the region of interest (ROI). $\mathcal{S}$ is a distance of similarity between I_r and I_d and $\mathcal{R}$ is a regularization term weighted by the factor λ. Under the assumption of the conservation of gray-levels (see optical flow problem [44]), $\mathcal{S}$ can be chosen as the squared L^2 norm of the residual of gray-levels which is equal to $I_r - I_d \circ (id + u)$, where $\circ$ refers to the composition operator between two functions and id to the identity function. In this case, $\mathcal{S}$ is defined by

$$\mathcal{S}(u, I_r, I_d) = \frac{1}{2}||I_r - I_d \circ (id + u)||^2_{L^2(\Omega)} = \frac{1}{2}\int_\Omega \left(I_r(x, y) - I_d((x, y) + u(x, y))\right)^2 dxdy. \tag{23}$$

The global approach, adopted in this work, considers the optimization over the whole region of interest in the contrary of local matching techniques that consist of performing the minimization over small sub-sets (see, *e.g.*, [72, 73] and [74] for a review of the different local matching techniques). In order to capture non-rigid deformations, we suggest using regular basis functions such as the B-spline functions of Section 2. This method, which has similarities with the FFD (free-form deformation) techniques [61], consists in deforming objects by manipulating a control point mesh. With this approach, the ROI is simply embedded in a cubic B-spline grid. It is defined by a set of two-dimensional control points. We denote the vector containing their coordinates $\mathbf{p} \in \mathbb{R}^{2n}$, where n is the number of control points. Denoting $\mathbf{u} \in \mathbb{R}^{2n}$ the vector of unknown displacements of the degrees of freedom, the displacement field on a spatial point $(x, y) \in \Omega$ is defined by the following linear combination:

$$u(x, y) = \mathbf{N}(x, y)\mathbf{u} \tag{24}$$

where $\mathbf{N}(x, y) \in \mathbb{R}^{2\times 2n}$ is the standard shape function matrix. Problem (23) can be viewed as a non-linear least squares problem and therefore can be solved numerically using a Gauss–Newton type algorithm [75, 76].

The problem of registering two images is ill posed due to multiple reasons. First, from a data view point, a pixel has only one information which is its gray level value but the unknown displacement for each pixel has two components. It results that there are more unknown variables than input variables. More generally, the convexity of the functional $\mathcal{S}$ is not guaranteed and depends of the nature of the images which leads to the non-unicity of the displacement solution. In addition to the treatment based on the Galerkin approximation (*i.e.*, given by the approximation space related to the basis functions gathered in $\mathbf{N}$), term $\mathcal{R}$ in (22) can help further regularizing the problem in challenging situations where the gray-level distribution is not sufficient, *i.e.* when the image gradient is either small or has a dominant direction, which is the case in this work. Such a term also allows to softly introduce a prior knowledge on the physics behind the deformation of the sample. Multiple approaches can be adopted in order to choose $\mathcal{R}$. A common choice used when dealing with cellular micro-structures, or in general irregular displacement fields, seems to be the use of Tikhonov regularization denoted $\mathcal{T}$ which consists in either minimizing large variations of the displacement components [77] or their gradients [61, 51, 50]. In this work, we will limit the use of this regularization scheme only to regions where no physical information is available. More precisely, we will consider the Tikhonov first order version that is based on:

$$\mathcal{T}(u) = \frac{1}{2}\int_\Omega \|\nabla u_x\|_2^2 + \|\nabla u_y\|_2^2 dxdy = \int_\Omega \left(\frac{\partial u_x}{\partial x}\right)^2 + \left(\frac{\partial u_x}{\partial y}\right)^2 + \left(\frac{\partial u_y}{\partial x}\right)^2 + \left(\frac{\partial u_y}{\partial y}\right)^2 dxdy. \tag{25}$$

The discrete form directly coming from $\mathcal{T}$ is given by:

$$\tilde{T}(\mathbf{u}) = \frac{1}{2}\int_\Omega \sum_{i=1}^{4} ||\mathbf{L}_i(x, y)\mathbf{u}||^2 dxdy = \frac{1}{2}\mathbf{u}^T\left(\int_\Omega \sum_{i=1}^{4} \mathbf{L}_i^T(x, y)\mathbf{L}_i(x, y)dxdy\right)\mathbf{u} = \frac{1}{2}\mathbf{u}^T\mathbf{L}\mathbf{u}, \tag{26}$$

where $\mathbf{L_i}$ are first order partial differential operators. $\mathbf{L}$ is called the Tikhonov linear operator. In order to properly select the DOF where the Tikhonov regularization will be applied, we will eventually consider a slightly different discrete cost function, based on the euclidean norm of the action of the Tikhonov operator instead of the scalar product:

$$\tilde{T}(\mathbf{u}) = \frac{1}{2}||\mathbf{L}\mathbf{u}||_2^2. \tag{27}$$

On the contrary, in the part of the ROI where physical information is available, we will rather use an elastic regularization that has proved to be efficient in the field of experimental solid mechanics [52, 46].

Indeed, as will be seen on the below numerical results, the previous Tikhonov regularization does not allow capturing physical strain fields because the regularization lacks of physical meaning. More precisely, this mechanically sound regularization scheme is based on the equilibrium gap method [52] whose discrete form reads:

$$\tilde{M}(\mathbf{u}) = \frac{1}{2}\|\mathbf{K}\mathbf{u} - \mathbf{f}\|_2^2, \tag{28}$$

where $\mathbf{K}$ and $\mathbf{f}$ are the stiffness matrix and vector force of the considered region, respectively. Practically, when acquiring images of deformed samples in solid mechanics, $\mathbf{f}$ can be reasonably assumed to be zero everywhere expect on the Dirichlet and non-zero Neumann boundaries. Indeed, we do not know well the distribution of the reaction forces or loading on such boundaries (we can only experimentally access to one component of the resultant force vector). That is why a special treatment of the boundaries on which $\mathbf{f}$ is not well known is considered. We denote Γ_d the union of these boundaries. In addition to the boundary control points, a stabilization is also used on the basis functions which have minimal values on the physical domain (*i.e.*, the cell struts). Overall, the control points regularized with the Tikhonov functional are the one defined by the index set $\mathcal{I}_T$ defined by:

$$\mathcal{I}_T = \{i/ \quad \mathbf{p}_i \in \Gamma_d \quad \text{and} \quad s(i) < tol << 1\} \quad \text{with} \quad s(i) = \frac{\displaystyle\int_{Supp(N_i^p)\cap\Omega_p} N_i^p(x,y)dxdy}{\displaystyle\int_{Supp(N_i^p)} N_i^p(x,y)dxdy} \in [0,1]. \tag{29}$$

We note that the selection criterion given by the function s defined in (29) depends on the considered geometry. The bigger the volume fraction the smaller s is chosen. For the geometry that will be studied in Section. 3.2 (see Fig. 19), we consider a tolerance value $tol = 10^{-3}$.

The considered optimization will consist in employing a Tikhonov regularization at the control points whose indices are in $\mathcal{I}_T$ and the mechanical equilibrium at the control points whose indices are in the complementary of $\mathcal{I}_T$. All in all, the discrete optimization problem is defined as follows:

$$\underset{\mathbf{u}\in\mathbb{R}^{2n}}{\arg\min}\left[S(\mathbf{u}) + \lambda_M M(\mathbf{u}) + \lambda_T T(\mathbf{u})\right], \tag{30}$$

where S is the Galerkin discretizations of $\mathcal{S}$ and T and M come from (27) and (28), respectively, and are defined such that:

$$T(\mathbf{u}) = \frac{1}{2}||\mathbf{D}_T\mathbf{L}\mathbf{u}||_2^2, \quad M(\mathbf{u}) = \frac{1}{2}||\mathbf{D}_M\mathbf{K}\mathbf{u}||_2^2, \tag{31}$$

where $\mathbf{D}_T$ and $\mathbf{D}_M$ are binary selection operators that respectively select the control points whose indices are in $\mathcal{I}_T$ and in its complementary. These two operators verify: $\mathbf{D}_T\mathbf{D}_M = \mathbf{0}$ and $\mathbf{D}_T + \mathbf{D}_M = \mathbf{I}$. λ_T and λ_M are parameters that are related to characteristic lengths that act as cut-off frequencies of two low-pass filters [46, 78]. It is important to note at this stage that the elastic behavior is not prescribed in a strong way, but in a weak sense with the help of the penalization factor λ_M. It is actually only used as a low pass filter to alleviate noise effects. As a result, the methodology does not appear in conflict with the measurement of kinematic fields exhibiting more complex, possibly anisotropic and non-linear, behaviors. In our case where the region observed represents a cellular material, the stiffness operator $\mathbf{K}$ is obtained by the automated, fairly priced, image-based model defined in Section 2.

The resolution of the regularized non-linear least squares problem (30) is performed using the following descent scheme:

$$\mathbf{u}^{(k+1)} = \mathbf{u}^{(k)} + \mathbf{d}^{(k)}, \tag{32}$$

where $\mathbf{d}^{(k)}$ is the solution of the following Gauss–Newton system:

$$\left(\mathbf{H}_S(\mathbf{u}^{(k)}) + \lambda_M\mathbf{H}_M(\mathbf{u}^{(k)}) + \lambda_T\mathbf{H}_T(\mathbf{u}^{(k)})\right)\mathbf{d}^{(k)} = -\left(\nabla S(\mathbf{u}^{(k)}) + \lambda_M\nabla M(\mathbf{u}^{(k)}) + \lambda_T\nabla T(\mathbf{u}^{(k)})\right) \tag{33}$$

and where $\mathbf{H}_S$ is an approximation using only first-order derivatives of the Hessian matrix of S. $\mathbf{H}_M$ and $\mathbf{H}_T$ are respectively the Hessian matrices of M and T and $\nabla_S, \nabla_M, \nabla_T$ are respectively the gradient vectors of S, M and T. The definition of these six operators is given by equations (34), (35), (36) and (37), see below:

$$\nabla S(\mathbf{u}^{(k)}) = -\int_\Omega \left(I_r(x,y) - I_d\left((x,y) + \mathbf{N}(x,y)\mathbf{u}^{(k)}\right)\right)\mathbf{N}(x,y)^T\nabla\mathbf{I_r}(x,y)dxdy; \tag{34}$$

$$\nabla M(\mathbf{u}^{(k)}) = \mathbf{K}^T\mathbf{D}_M^T\mathbf{D}_M\mathbf{K}\mathbf{u}^{(k)}, \quad \nabla T(\mathbf{u}^{(k)}) = \mathbf{L}^T\mathbf{D}_T^T\mathbf{D}_T\mathbf{L}\mathbf{u}^{(k)}; \tag{35}$$

$$\mathbf{H}_S(\mathbf{u}^{(k)}) = \int_\Omega \mathbf{N}(x,y)^T(\nabla\mathbf{I_d})\left((x,y)+\mathbf{N}(x,y)\mathbf{u}^{(k)}\right)^T(\nabla\mathbf{I_d})\left((x,y)+\mathbf{N}(x,y)\mathbf{u}^{(k)}\right)\mathbf{N}(x,y)dxdy; \tag{36}$$

$$\mathbf{H}_M = \mathbf{K}^T\mathbf{D}_M^T\mathbf{D}_M\mathbf{K}, \quad \mathbf{H}_T = \mathbf{L}^T\mathbf{D}_T^T\mathbf{D}_T\mathbf{L}. \tag{37}$$

Practically, the descent direction $\mathbf{d}^{(k)}$ is obtained by approximating $\nabla\mathbf{I_d}\circ(id+u)$ by $\nabla\mathbf{I_r}$. This approximation was discussed in [76, 79]. In this case, the matrix $\mathbf{H}_S$ does not depend on the displacement $\mathbf{u}^{(k)}$ and the left hand side of the Gauss–Newton linear system is assembled only once in a pre-processing step. Even more interestingly, the left-hand side can be factorized in a pre-processing step so that only triangular systems need to be solved at each DIC iteration. As a consequence, the incorporation of the stiffness matrix $\mathbf{K}$ for the mechanically regularized scheme does not add significant extra cost during the DIC algorithm. Only the right-hand side is updated during the descent iterations. The integration of the terms in (34)-(35)-(36)-(37) is performed using a rectangle integration with a subdivision length equal to the element resolution, *i.e.* a number of integration points in one element equal to the number of its pixels [80]. The optimization algorithm is stopped using a stagnation criteria defined by

$$\frac{||\mathbf{u}^{(k+1)}-\mathbf{u}^{(k)}||_2}{||\mathbf{u}^{(k+1)}||_2} < 10^{-3}. \tag{38}$$

In order to measure the registration quality of the displacement solution, we consider the dimensionless correlation residual equal to the standard deviation of the residual of gray-levels divided by the dynamic of the initial image I_r:

$$\eta = \frac{1}{\max I_r - minI_r} std(I_r - I_d\circ(id+u)), \quad \text{where} \quad std(h) = \sqrt{\bar{h^2}-\left(\bar{h}\right)^2}, \quad \bar{h} = \frac{1}{\mathcal{A}(\Omega)}\int_\Omega h d\Omega, \tag{39}$$

and where $\mathcal{A}(\Omega)$ is the area of the region of interest.

Regarding the initialization of the Gauss–Newton algorithm, it is common to use efficient and fast strategies for finding the initial guess $\mathbf{u}^{(0)}$. The idea is to rapidly reach a displacement field that satisfies small values of the residual of gray-levels. In the next numerical examples, the initial guess $\mathbf{u}^{(0)}$ is the vector equal to zero. Multiple initialization strategies exist in the literature. We list for example the maximization of the cross-correlation function in the Fourier space using the Fast Fourier Transform (FFT) [40], the use of coarse to fine schemes and multi-level strategies [81, 82] (see section 3.2.1 for a multi-level mesh refinement strategy) or optimal transport for diffeomorphic registration [83].

In order to improve the Tikhonov regularization at the boundaries, we suggest considering an iterative procedure in which the weight of the parameter λ_T is reduced after each optimization in order to attain small correlation residuals. A summary of the DIC algorithm in addition to this iterative procedure are detailed in Algorithm 1.

Algorithm 1 Registration algorithm

Input data:

- Images I_r and I_d

User defined input parameters:

- Region of interest. It defines the domain Ω
- Image sub-pixel evaluation method (here: cubic B-spline smoothing defined in (1)-(2))
- Discretization length of the B-spline elements (fixed by the accuracy of the DIB model)
- Degree of the B-spline functions (as seen in Section 2, we consider cubic B-splines for non-rigid transformations)
- Regularization parameters: λ_T and λ_M (see (30))
- Mechanical model's parameters: tentative Young's modulus E, tentative Poisson coefficient ν, the fictitious domain method penalization parameter α_f defined in (5) and the threshold value g_t for constructing the geometry level-set.
- Initial guess $\mathbf{u}^0$ (Here set to zero)

Gauss–Newton algorithm:

function REGISTRATE($\mathbf{u}^0$, λ_M, λ_T)
Runs the Gauss-Newton algorithm defined in (32)-(33)
return $\mathbf{u}^{(*)}, \eta,$ where $\mathbf{u}^{(*)}$ is the solution at convergence and η is the correlation residual defined in (39).

Multi-level Tikhonov regularization algorithm:

$k = 0$
$\mathbf{u}^{(k)} = \mathbf{0}$
while *Residual difference* < 0 **do**
$\mathbf{u}^{(k+1)}, \eta^{k+1} =$ REGISTRATE$(\mathbf{u}^{(k)}, \lambda_M, \lambda_T)$
Reduce Tikhonov regularization parameter λ_T
Residual difference $= \eta^{k+1} - \eta^k$
$k = k + 1$
Optimal solution $= \mathbf{u}^{(k-1)}$

Remark 3. *An important question in DIC is the sub-pixel evaluation of images. Due to the discontinuous nature of images, interpolation can induce non-negligible errors. The evaluation of the image on physical points can be performed with various strategies such as nearest-neighbor evaluation, bi-linear interpolation or bi-cubic spline interpolation. In order to decrease interpolation errors and increase the regularization of the DIC problem, it is possible to blur the reference and deformed images I_r and I_d by filtering them using a Gaussian filter. This means that the new unknown displacement is searched for such that $(G_\sigma * I_r) = (G_\sigma * I_d) \circ (id + u)$, where G_σ is a Gaussian kernel for example. In order to evaluate the images I_r and I_d we suggest using the cubic B-spline description defined in* (1)-(2) *which approximates a Gaussian filter [10]. This same strategies had been used in [37] for efficient gradient computation in image registration. This allows us to perform in the same time, the blur of the images, the sub-pixel evaluation of the image and its gradient, and the construction of the level-set description of the observed cellular material.*

3.2. Numerical example: application to a synthetic cellular material

We assess in this part, the performance of the developed DIC algorithm. To do so we consider a set of synthetic images representing a cellular material with a complex micro-structure composed of several random holes. The micro-structure's geometry is similar to a slice of a cellular foam. Regarding the material behavior at the micro-scale, although it may be very complex in practice (anisotropic, elasto-plastic, etc.), we consider in this preliminary work a simple, isotropic, linear elastic constitutive law with Young's modulus and Poisson coefficient set to $E = 73.1 \times 10^9 Pa$ and $\nu = 0.33$, respectively.

Our objective in what follows is to measure local strain fields in this regime, which is not possible with standard approaches. In order to validate the results of the registration algorithm, we will conduct a comparison of the strain field obtained from the suggested algorithm with the strain field of a reference finite element solution. Fig. 19a shows a finite element mesh of the exact geometry on which we consider a compression test under plane stress assumption. A displacement of value $u_0 = -3 \times 10^{-3}\ m$ is imposed in the x direction at the right boundary. The left boundary is fixed. The corresponding global longitudinal strain at the right boundary is equal to $\varepsilon_{xx} \approx 2.72\%$. The finite element solution is displayed in Fig. 20. In the following numerical tests, we will confront the results of the registration algorithm with the solutions coming from the finite element calculation of Fig. 19. For each test, we will display the euclidean norm of the displacement field and the Von Mises strain defined in (21).

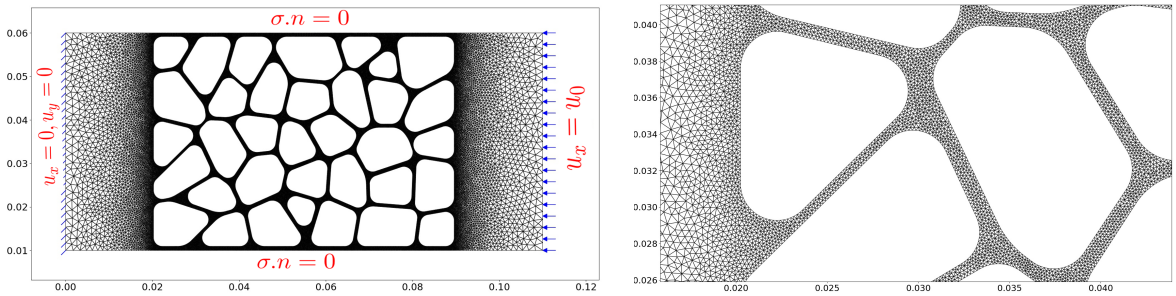

(a) Mechanical problem.

(b) Zoom on a region of Fig. 19a

Figure 19: Virtual finite element test.

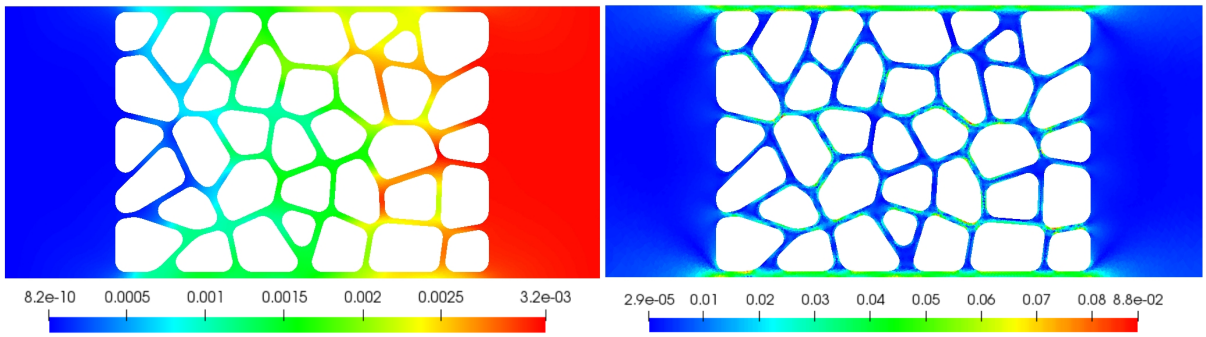

(a) Euclidean norm of the displacement field.

(b) Von Mises strain norm.

Figure 20: Finite element solution of the problem of the mechanical problem defined in Fig. 19a.

The input data of the DIC problem, which are the reference and deformed images I_r and I_d are generated from a pixelation of the finite element mesh of Fig. 19 before and after deformation. More precisely, the images are created by generating very high resolution binary images and afterwards down-sampling them by pixel aggregation. They are shown in Fig. 21 with a chosen ROI. The acquisition of the images is a crucial step from a practical point of view. In addition to noise and distortion for two-dimensional images or artifacts for volume images, an important parameter is the image resolution. The chosen resolution is such that the number of pixels in the cell struts is equivalent to the smallest geometric thickness of the real acquisition of a closed-cell foam with a low resolution μ-CT scan set. In the images of Fig. 21, we have approximately 4 pixels in the cell struts thickness. As the dimensions of the true specimen are known, we assign to the pixel a physical dimension, therefore the image space is the physical space with the same unit as the specimen shown in Fig. 19a. In general, the displacement field is expressed in pixel units. However, depending on the experimental setup, it is possible to estimate the pixel size using the information given by the camera-setup or the μ-CT scanner.

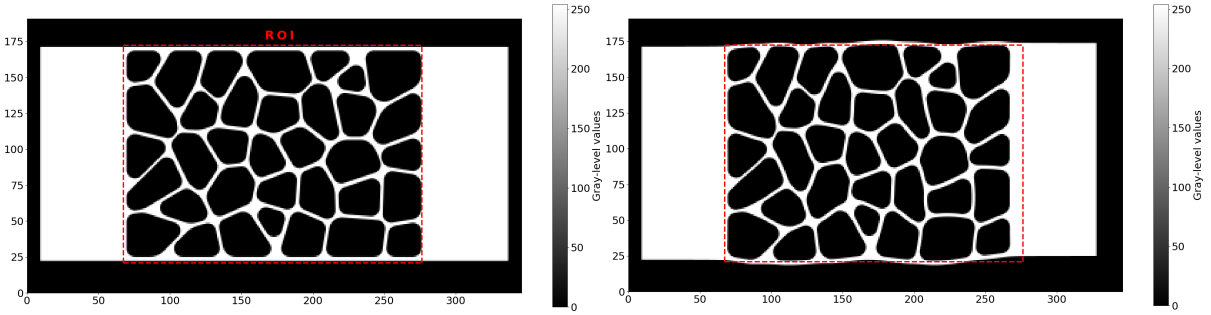

(a) Reference configuration: image I_r.

(b) Deformed configuration: image I_d.

Figure 21: DIC inputs resulting from a virtual compression test.

As mentioned in Eq. (24), the unknown displacement field is searched in the B-spline space. It results that the B-spline domain is simply defined over a user-defined region of interest (see Fig. 21 for an example of a ROI).

We will test the three following B-spline DIC cases: a case where no regularization term is added, a case using only Tikhonov regularization on the whole ROI and finally our approach using a mechanical regularization (except on the Dirichlet boundaries where the Tikhonov regularization is used).

3.2.1. Global B-spline DIC without external regularization

We set here $\lambda_T = \lambda_M = 0$ in (30). The only regularization considered in this case is the B-spline approximation of the displacement field. Therefore the B-spline element size determines the amount of regularization used [46]. When considering cubic B-splines, the idea is to start by a mesh and gradually decrease the elements size as suggested in [81]. Using the knot insertion algorithm for B-splines, it is possible to define a refinement operator for going from a coarse displacement field to a refined one (see [84, 85] for more details of the knot insertion algorithm). This grid refinement strategy detailed for example in [86] can be applied to large variety of inverse problems. It has been recently applied in [87] for solving for example the shape measurement problem in setero-DIC. A multi-level refinement approach is summarized in Algorithm 2. Starting from a coarse mesh (see Fig. 22a), large disparities are corrected gradually in order to capture more local displacement fields. The solution of the registration algorithm is displayed in Fig. 23.

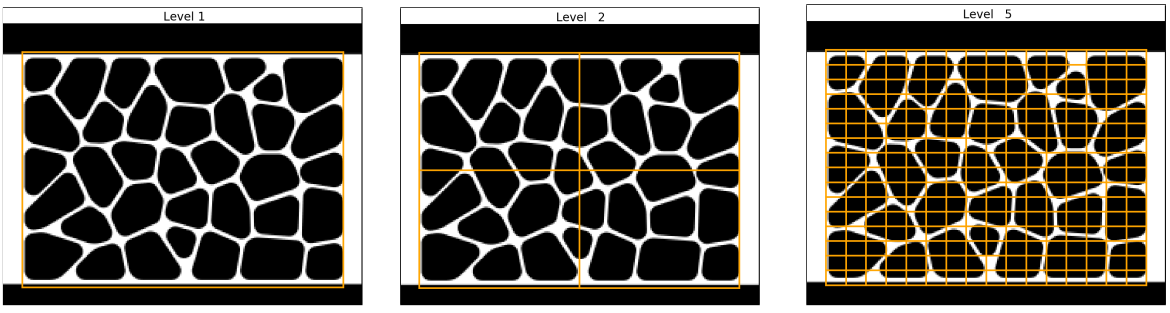

(a) $2^0 \times 2^0$ elements.

(b) $2^1 \times 2^1$ elements.

(c) $2^4 \times 2^4$ elements.

Figure 22: Multi-level refinement scheme using cubic B-splines. At each step, the orange grid represents the B-spline grid defined over the region of interest.

Algorithm 2 Multi-level refinement based on one scale of image resolution

Multi-level algorithm:

$k = 0$
$\mathbf{u}^{(k)} = \mathbf{u}^{(i)} = \mathbf{0}$
REGISTRATE$(\mathbf{u}^{(k)}, \lambda_M = 0, \lambda_T = 0)$
while *Residual difference* < 0 **do**
  Refine B-spline mesh by decreasing element length (dividing by 2 the element length).
  Perform the mapping from the coarse mesh to the fine mesh:
  $\mathbf{u}^{(i)} = \mathbf{C}^T \mathbf{u}^{(k)}$ where $\mathbf{C}$ is the knot refinement operator.
  $\mathbf{u}^{(k+1)}, \eta^{k+1} =$ REGISTRATE$(\mathbf{u}^{(i)}, \lambda_M = 0, \lambda_T = 0)$ (see definition of REGISTRATE in Algorithm 1).
  Residual difference $= \eta^{k+1} - \eta^k$
  $k = k + 1$
Optimal solution $= \mathbf{u}^{(k-1)}$

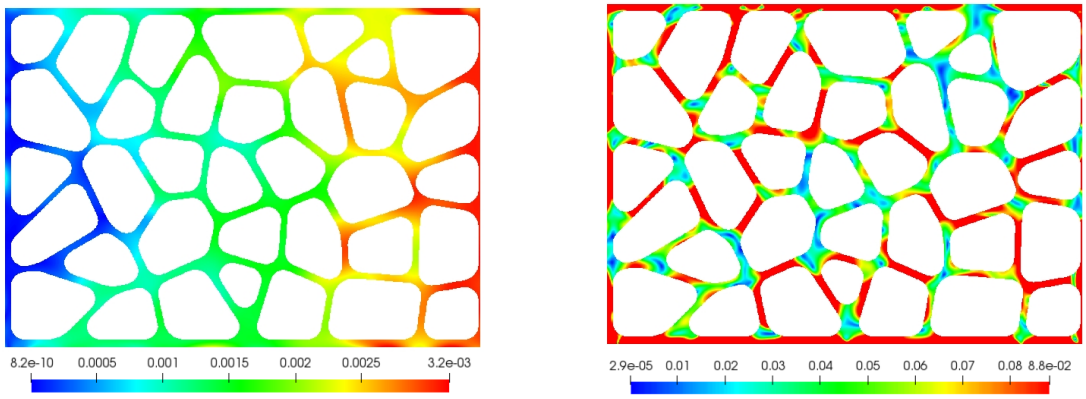

(a) Euclidean norm of the displacement field.

(b) Von Mises strain norm.

Figure 23: Solution of the global method without any penalization using a multi-level refinement strategy.

With the multi-level refinement approach, a correlation residual $\eta = 0.77\%$ is attained. This residual is reached at a level of 4 subdivisions corresponding to the mesh shown in Fig. 22c and in which the element resolution is equal to $\sqrt{(hx/\Delta x)(hy/\Delta y)} \approx 11.11$ pixels, where $h_x, h_y, \Delta x, \Delta y$ are respectively the element size and the pixel size in x and y directions. Beyond this mesh resolution, the algorithm diverges and becomes unstable. The displacement field solution has the same homogeneity as the finite element solution, however, the differentiation of the solution, gives a strain field solution that presents high strain concentrations with values that drastically surpass the reference finite element strain field (see Fig. 23 in comparison to Fig. 20).

3.2.2. B-spline DIC with only Tikhonov regularization

We consider in this case a classic Tikhonov regularization by setting $\lambda_M = 0$. Here, the regularization acts on all the control points, so we set $\mathbf{D}_T = \mathbf{I}$ in (31). Using the Tikhonov parameter reduction strategy shown in Algorithm 1, λ_T is varied from 10^5 to 10^1. When using this regularization, the Gauss–Newton algorithm converges independently of the element size. When considering for example a mesh that has an element size equal to 4.74 pixels (see Fig. 25), which is the same mesh resolution that will be used for the mechanical regularization in the next section, we obtain at convergence the following residuals: $\eta = 3.62\%$ for $\lambda = 10^5$, $\eta = 0.93\%$ for $\lambda = 10^4$, $\eta = 0.49\%$ for $\lambda = 10^3$, $\eta = 0.38\%$ for $\lambda = 10^2$ and $\eta = 0.34\%$ for $\lambda = 10^1$. This numerically confirms the existing trade-off between the conservation of gray-levels and the regularity of the solution given by the cost function (30). However, in all cases, the registered solution using this type of regularization presents high strain concentrations in the cell struts (see Fig. 24). It thus seems that the Tikhonov regularization enables to get a good solution in terms of residuals but the solution clearly does not live in a mechanically consistent space.

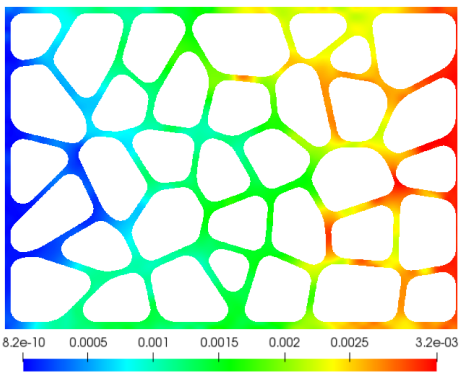

(a) Euclidean norm of the displacement field for $\lambda_T = 10^1$.

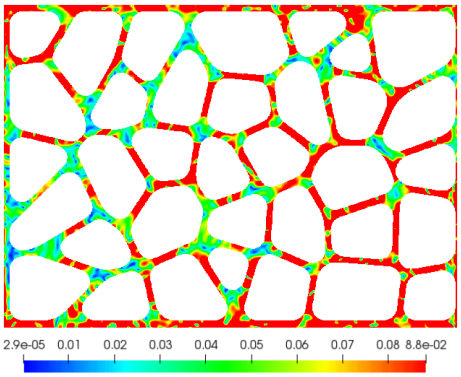

(b) Von Mises strain norm for $\lambda_T = 10^1$.

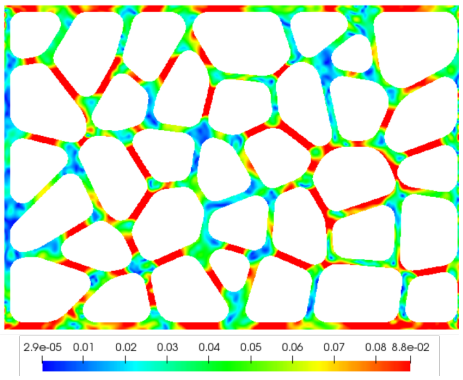

(c) Von Mises strain norm for $\lambda_T = 10^3$.

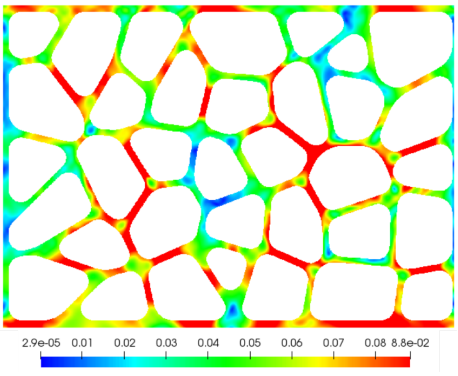

(d) Von Mises strain norm for $\lambda_T = 10^5$.

Figure 24: Solution using the multi-level Tikhonov regularization.

3.2.3. B-spline DIC with FCM-based Mechanical regularization

Finally we consider the mechanical regularization scheme with all the regularization terms: $\lambda_T \neq 0$ and $\lambda_M \neq 0$. λ_M and λ_T are fixed in an iterative way similarly to the one detailed in the Multi-level Tikhonov regularization algorithm (see Algorithm 1). As mentioned in Eq.(29), a Tikhonov regularization is applied to the control points belonging to the index set $\mathcal{I}_T$ (see Eqs. (30)-(31)). For the B-spline grid, we take the same discretization as the one which enabled to get our fairly priced image-based mechanical model in Section 2, so that we are optimal in terms of computational cost and accuracy. Obviously, we could consider larger elements for the B-spline mesh and still make the algorithm converge thanks to the mechanical regularization. However, we would obtain less accurate results in this case since the B-spline mesh would be too coarse to properly describe the mechanical behavior at the sub-cellular scale of the sample. The chosen mesh here has an element size equal to 4.74 pixels and is displayed in Fig. 25.

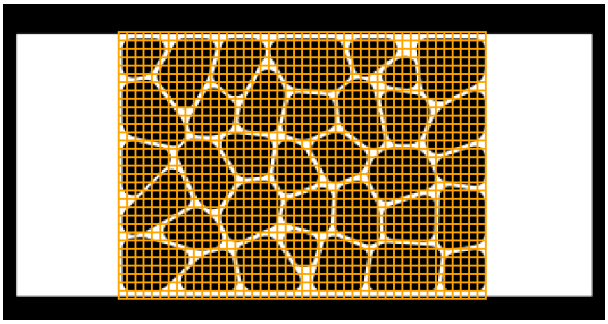

Figure 25: B-spline mesh defined for solving the DIC problem.

As explained previously, the mechanical regularization term M is defined by the stiffness operator $\mathbf{K}$ which describes the elastic behavior of the ROI. A choice thus needs to be done for the associated material's mechanical parameters E and ν. Here, we take the same parameters as the ones assumed

for the behavior of the true micro-structure. However, we emphasize that since the stiffness matrix is proportional to E, E has no effect on the regularization. In addition, we conducted different numerical tests with different Poisson ratios (ranging from 0.1 to 0.5) for the regularization term. Indistinguishable results were obtained which is consistent since, once again, the elastic behavior in the regularization is prescribed in a weak sense, only to alleviate noise effects in DIC. More precisely, the obtained solution fields are shown in Fig. 26.

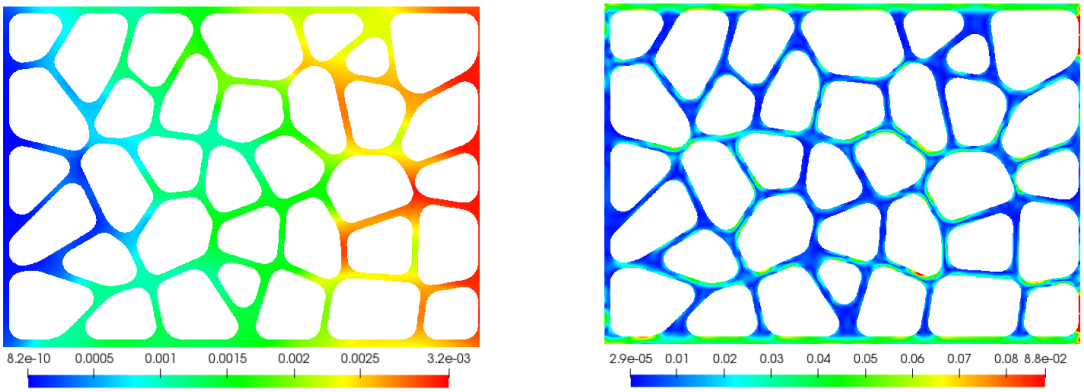

(a) Euclidean norm of the displacement field.

(b) Von Mises strain norm.

Figure 26: Solution using the equilibrium gap regularization.

With $\lambda_M = 10^{-11}$, the displacement field solution achieved a correlation residual $\eta = 0.72\%$. We observe in Fig. 26, that the strain field solution is very close to the one used for generating the images I_r and I_d at the bulk of the sample. Thanks to the high accuracy of the mechanical model, regular and local bendings are observed at the cellular beams (see Fig. 27). This shows that, under elastic deformations, the suggested mechanical regularization surpasses the two previous DIC methods and allows to estimate local strain fields at the sub-cellular scale. These results appear very promising for the long-term goal of treating real 3D image data. It is worth noting again that the present situation is very challenging given the poor textures considered (no speckle pattern and only about three pixels per strut), which may make most of today correlation strategies fail.

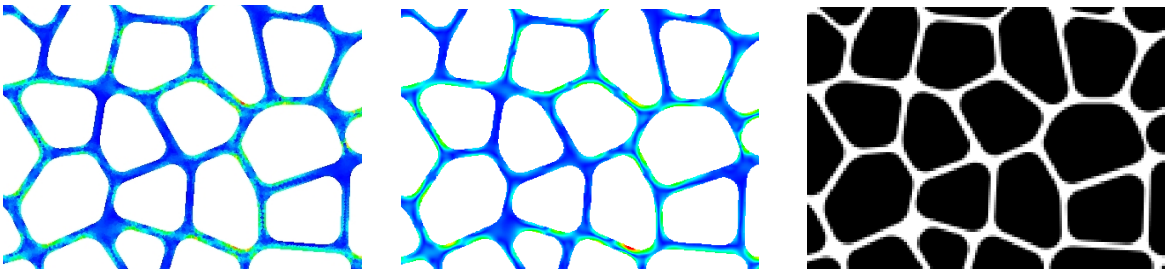

(a) Strain norm of the finite element simulation.

(b) Strain norm of the registered solution.

(c) Reference image I_r.

Figure 27: Zoom on a region in the ROI.

In order to quantify the measurement error of the different DIC approaches, we consider the uncertainty of the measurements. As the reference FE solution that is used to advect the reference image I_r is known and defined over the FE mesh depicted in Fig.19, the comparison between the measured field denoted F^{mes} and the reference field denoted F^{fem} is not immediate. In fact, the two fields are defined over two different geometries, *i.e.* the level-set geometry and the FE mesh geometry. The measurement error is therefore computed on a point cloud belonging to the intersection of the two geometries. Denoting n_p the number of points belonging to the intersection of the two domains, we consider the measurement uncertainty:

$$S(F) = \sqrt{\frac{1}{n_p - 1} \sum_{i=1}^{n_p} \left(F_i^{mes} - F_i^{fem} \right)^2}. \tag{40}$$

In the above equation, each component F_i stands for the evaluation of the field of interest at each interrogation point of the point cloud. We report the uncertainty for each method in Tab. 2. These results clearly show that the mechanically regularized method is the most precise in terms of measurements of displacement and strain fields compared to the two standard DIC methods. In addition, when using standard methods (with or without Tikhonov regularization), it can be observed that the strain measurement uncertainty is always greater than the reference strain we want to measure, which proves quantitatively what could be observed qualitatively on Figs. 23 and 24.

	$S(u_x)$ (pixels)	$S(u_y)$ (pixels)	$S(\varepsilon_{vm})$
Standard multi-level DIC	4.5×10^{-1}	1.9×10^{-1}	1.9×10^{-1}
Tikhonov regularization	1.6×10^{-1}	1.1×10^{-1}	5×10^{-2}
Mechanical regularization	2×10^{-2}	3×10^{-2}	4.7×10^{-3}

Table 2: Uncertainty of the measurements.

3.2.4. Noise sensitivity analysis

In classical 2D imaging, the noise sensitivity of the DIC algorithm is usually studied by considering a white noise, *i.e.* more precisely, by perturbing the images I_r and I_d with a random Gaussian variable of zero mean and with a standard deviation $\sigma \in \{0, 1, 2, 3\}$ gray-levels. For each value of σ, 10 random variables are generated. We therefore consider the mean uncertainty over these 10 random tests. Figs. 28a-28b show, respectively, the evolution of the global displacement uncertainty defined by $\langle \frac{1}{2}(S(u_x) + S(u_y)) \rangle$ and of the Von Mises strain uncertainty $\langle S(\varepsilon_{vm}) \rangle$ with respect to the noise standard deviation. $\langle . \rangle$ stands for the mean over the 10 noise tests and S is defined in Eq. (40). No significant error change is observed with respect to noise (same value along the Y axis). This is consistent with Remark 3: the sub-pixel evaluation based on the smooth representation defined in (1)-(2) appears to act as a pre-filter for the images, which is another interest of our combined image-based model — DIC approach.

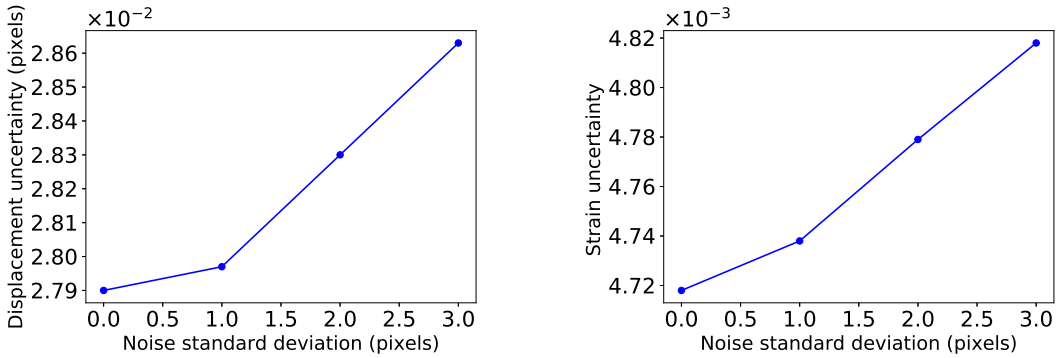

(a) Evolution of the displacement uncertainty in pixel unit.

(b) Evolution of the Von Mises strain uncertainty.

Figure 28: Noise sensitivity analysis for fixed regularization parameters.

We should note that other more complex noises can be encountered in 3D image acquisitions (we can quote, for example, ring artifacts and beam hardening [88]). That is why, acquired images are generally pre-processed with noise reduction algorithms.

4. Conclusion and perspectives

In the first part of this work, we attempt to shed a new quantitative light on the construction of proper unfitted image-based models. More precisely, a special care is taken to analyze the numerical approximation error while taking into account the intrinsic geometry error resulting from the image generation process (sampling + quantization). This study thus breaks with the usual practice in the field where the modeling error and the convergence of numerical methods are most of the time assessed with geometries deemed to be exact, which is not the case with image-based models in general. By means of various two-dimensional numerical experiments, we show that, in addition to being dependent on the modeling parameters (element size, polynomial degrees, quadrature rule), the numerical approximation error is

related to the pixel size which controls the intrinsic geometry error. More specifically, the geometry error propagates into a mechanical model error and, in turn, into an error on the measured fields from DIC. In this context, we propose rules that allow for automatic determination of the discretization parameters. For the quadrature rule in particular, the number of integration sub-cells is adjusted according to the definition of the images in order to achieve asymptotic precision with a minimal computational effort. Then the polynomial degree and element size can be properly chosen to reach the best possible accuracy while avoiding excessive and unnecessary calculations. In particular, it is shown that we do not need to go to higher orders than $p = 3$, while it is often stated in the literature (see, *e.g.*, [9, 30]). In that sense, the resulting image-based model is characterized as a fairly-priced model. The model constructed in this way is far more accurate with up to an order of magnitude less number of unknowns compared to all other classical (boundary fitted) approaches considered (Marching squares, Voxel-based with segmentation or with mechanical properties related to gray-levels).

In the second part of this work, we show that it is possible to estimate displacements and their derivatives within the strut thickness of a mechanically stressed cellular sample using Digital Image Correlation without texture at the sub-cell scale. No classical method of the literature has been able to correctly estimate local strains. Therefore our approach, consisting in exploiting the sample-specific model and the image gradient information contained in the domain boundaries by a DIC-type metric, appears as a promising strategy to investigate the mechanics of structured materials at their micro-structural scale. To some extent, our strategy shares many similarities with the newly-introduced mechanical shape correlation [89], although the latter requires greater confidence in the mechanical model.

The main perspectives of this work is to apply this approach to real experiments on cellular samples and to generalize the approach to three-dimensional images. First, in terms of application, this undoubtedly goes with the extension of the proposed methodology to measure and identify the plastic behavior at the sub-cellular scale. Even if the considered regularization is based on a simple elastic behavior, it has to be noted here that it is not incompatible with the measurement of more complex non-linear phenomena. Indeed, the elastic behavior is not prescribed in a strong way, but in weak sense. The elastic model is actually only used as a low-pass filter to alleviate noise effects. This framework thus appears promising also in the non-linear context and could be complemented by other existing devices to address the mechanical characterization at the sub-cellular scale (see, *e.g.*, [90] for damage and [91] for elasto-plastic regimes). Then, from an algorithmic point of view, the following research axes might be pursued for the generalization to 3D. The level-set coefficients a_i defined in (2) could be substituted by the gray-level input data directly to reduce memory requirements in 3D (see, *e.g.*, [92]). Then, in order to treat large scale Digital Volume Correlation problems, dedicated domain coupling methods such as those suggested in [93, 94] could be used for the development of parallel domain decomposition solvers. Furthermore, other methods based on low-dimension approximation such as the proper generalized decomposition (which is particularly appropriate considering the tensor structure of B-Splines) [95, 17, 96] could help further reducing the computational cost of the DVC algorithm. In this trend, iterative solvers for unfitted methods [10, 97, 98, 32] could also be considered for realistic three-dimensional generalization.

Finally, a series of other prospects could also be envisioned such as adaptive refinement for materials with multi-scale micro-structures [10, 36], extension to multi-phase (> 2) materials using more advanced modellings such as those based on the Cut-FEM method [28]. In addition, we recall that the threshold value used for characterizing the geometric level-set is a user-defined parameter herein and is one of the crucial parameters. Experimental calibration strategies or acquiring multiple images of the material sample could help minimizing the uncertainties related to both threshold and interpolation.

Funding acknowledgments

This work was supported by *Région Occitanie* and *Université Fédérale Toulouse-Midi-Pyrénées*.

References

[1] M. Ashby, Y. J. Bréchet, Designing hybrid materials, Acta materialia 51 (2003) 5801–5821.

[2] D. Ulrich, B. van Rietbergen, H. Weinans, P. Rüegsegger, Finite element analysis of trabecular bone structure: a comparison of image-based meshing techniques, Journal of Biomechanics 31 (1998) 1187 – 1192.

[3] B. van Rietbergen, H. Weinans, R. Huiskes, A. Odgaard, A new method to determine trabecular bone elastic properties and loading using micromechanical finite-element models, Journal of biomechanics 28 (1995) 69–81.

[4] E. Maire, A. Fazekas, L. Salvo, R. Dendievel, S. Youssef, P. Cloetens, J. M. Letang, X-ray tomography applied to the characterization of cellular materials. related finite element modeling problems, Composites science and technology 63 (2003) 2431–2443.
[5] N. Moës, M. Cloirec, P. Cartraud, J.-F. Remacle, A computational approach to handle complex microstructure geometries, Computer Methods in Applied Mechanics and Engineering 192 (2003) 3163 – 3177. Multiscale Computational Mechanics for Materials and Structures.
[6] G. Legrain, P. Cartraud, I. Perreard, N. Moës, An x-fem and level set computational approach for image-based modelling: Application to homogenization, International Journal for Numerical Methods in Engineering 86 (2011) 915–934.
[7] W. D. Lian, G. Legrain, P. Cartraud, Image-based computational homogenization and localization: comparison between x-fem/levelset and voxel-based approaches, Computational Mechanics 51 (2013) 279–293.
[8] M. Ruess, D. Tal, N. Trabelsi, Z. Yosibash, E. Rank, The finite cell method for bone simulations: verification and validation, Biomechanics and modeling in mechanobiology 11 (2012) 425–437.
[9] A. Düster, H.-G. Sehlhorst, E. Rank, Numerical homogenization of heterogeneous and cellular materials utilizing the finite cell method, Computational Mechanics 50 (2012) 413–431.
[10] C. Verhoosel, G. van Zwieten, B. van Rietbergen, R. de Borst, Image-based goal-oriented adaptive isogeometric analysis with application to the micro-mechanical modeling of trabecular bone, Computer Methods in Applied Mechanics and Engineering 284 (2015) 138 – 164. Isogeometric Analysis Special Issue.
[11] L. Giovannelli, J. Ródenas, J. Navarro-Jiménez, M. Tur, Direct medical image-based finite element modelling for patient-specific simulation of future implants, Finite Elements in Analysis and Design 136 (2017) 37 – 57.
[12] X. Liu, J. Réthoré, M.-C. Baietto, P. Sainsot, A. A. Lubrecht, An efficient strategy for large scale 3d simulation of heterogeneous materials to predict effective thermal conductivity, Computational Materials Science 166 (2019) 265 – 275.
[13] J.-Y. Buffiere, E. Maire, J. Adrien, J.-P. Masse, E. Boller, In situ experiments with x ray tomography: an attractive tool for experimental mechanics, Experimental mechanics 50 (2010) 289–305.
[14] B. K. Bay, T. S. Smith, D. P. Fyhrie, M. Saad, Digital volume correlation: three-dimensional strain mapping using x-ray tomography, Experimental mechanics 39 (1999) 217–226.
[15] S. J. Hollister, J. Brennan, N. Kikuchi, A homogenization sampling procedure for calculating trabecular bone effective stiffness and tissue level stress, Journal of Biomechanics 27 (1994) 433–444.
[16] J. Homminga, R. Huiskes, B. Van Rietbergen, P. Rüegsegger, H. Weinans, Introduction and evaluation of a gray-value voxel conversion technique, Journal of Biomechanics 34 (2001) 513–517.
[17] L. Gomes Perini, J.-C. Passieux, J.-N. Périé, A multigrid pgd-based algorithm for volumetric displacement fields measurements, Strain 50 (2014) 355–367.
[18] P. Frey, B. Sarter, M. Gautherie, Fully automatic mesh generation for 3-d domains based upon voxel sets, International Journal for Numerical Methods in Engineering 37 (1994) 2735–2753.
[19] A. Düster, J. Parvizian, Z. Yang, E. Rank, The finite cell method for three-dimensional problems of solid mechanics, Computer Methods in Applied Mechanics and Engineering 197 (2008) 3768 – 3782.
[20] T. Hoang, C. V. Verhoosel, C.-Z. Qin, F. Auricchio, A. Reali, E. H. van Brummelen, Skeleton-stabilized immersogeometric analysis for incompressible viscous flow problems, Computer Methods in Applied Mechanics and Engineering 344 (2019) 421–450.
[21] J. Parvizian, A. Düster, E. Rank, Finite cell method, Computational Mechanics 41 (2007) 121–133.
[22] A. Embar, J. Dolbow, I. Harari, Imposing dirichlet boundary conditions with nitsche's method and spline-based finite elements, International journal for numerical methods in engineering 83 (2010) 877–898.
[23] D. Schillinger, E. Rank, An unfitted hp-adaptive finite element method based on hierarchical b-splines for interface problems of complex geometry, Computer Methods in Applied Mechanics and Engineering 200 (2011) 3358–3380.
[24] E. Burman, S. Claus, P. Hansbo, M. G. Larson, A. Massing, Cutfem: Discretizing geometry and partial differential equations, International Journal for Numerical Methods in Engineering 104 (2015) 472–501.
[25] C. Lehrenfeld, High order unfitted finite element methods on level set domains using isoparametric mappings, Computer Methods in Applied Mechanics and Engineering 300 (2016) 716–733.
[26] T.-P. Fries, S. Omerović, Higher-order accurate integration of implicit geometries, International Journal for Numerical Methods in Engineering 106 (2016) 323–371.
[27] G. Legrain, N. Moes, Adaptive anisotropic integration scheme for high-order fictitious domain methods: Application to thin structures, International Journal for Numerical Methods in Engineering 114 (2018) 882–904.
[28] P. Kerfriden, S. Claus, I. Mihai, A mixed-dimensional cutfem methodology for the simulation of fibre-reinforced composites, Advanced Modeling and Simulation in Engineering Sciences 7 (2020) 1–26.
[29] D. Schillinger, L. Dede, M. A. Scott, J. A. Evans, M. J. Borden, E. Rank, T. J. Hughes, An isogeometric design-through-analysis methodology based on adaptive hierarchical refinement of nurbs, immersed boundary methods, and t-spline cad surfaces, Computer Methods in Applied Mechanics and Engineering 249 (2012) 116–150.
[30] D. Schillinger, M. Ruess, The finite cell method: A review in the context of higher-order structural analysis of cad and image-based geometric models, Archives of Computational Methods in Engineering 22 (2015) 391–455.
[31] D. Kamensky, M.-C. Hsu, D. Schillinger, J. A. Evans, A. Aggarwal, Y. Bazilevs, M. S. Sacks, T. J. Hughes, An immersogeometric variational framework for fluid–structure interaction: Application to bioprosthetic heart valves, Computer Methods in Applied Mechanics and Engineering 284 (2015) 1005 – 1053. Isogeometric Analysis Special Issue.
[32] F. de Prenter, C. Verhoosel, G. van Zwieten, E. van Brummelen, Condition number analysis and preconditioning of the finite cell method, Computer Methods in Applied Mechanics and Engineering 316 (2017) 297 – 327. Special Issue on Isogeometric Analysis: Progress and Challenges.
[33] D. Elfverson, M. G. Larson, K. Larsson, A new least squares stabilized nitsche method for cut isogeometric analysis, Computer Methods in Applied Mechanics and Engineering 349 (2019) 1 – 16.
[34] T. Elguedj, J. Réthoré, A. Buteri, Isogeometric analysis for strain field measurements, Computer Methods in Applied Mechanics and Engineering 200 (2011) 40 – 56.

[35] S. M. Kleinendorst, J. P. M. Hoefnagels, C. V. Verhoosel, A. P. Ruybalid, On the use of adaptive refinement in isogeometric digitalimage correlation, International Journal for Numerical Methods in Engineering 104 (2015) 944–962.
[36] A. Pawar, Y. Zhang, Y. Jia, X. Wei, T. Rabczuk, C. L. Chan, C. Anitescu, Adaptive fem-based nonrigid image registration using truncated hierarchical b-splines, Computers & Mathematics with Applications 72 (2016) 2028–2040.
[37] C. L. Chan, C. Anitescu, Y. Zhang, T. Rabczuk, Two and three dimensional image registration based on b-spline composition and level sets, Communications in Computational Physics 21 (2017) 600–622.
[38] E. Verhulp, B. van Rietbergen, R. Huiskes, A three-dimensional digital image correlation technique for strain measurements in microstructures, Journal of biomechanics 37 (2004) 1313–1320.
[39] N. Lenoir, M. Bornert, J. Desrues, P. Bésuelle, G. Viggiani, Volumetric digital image correlation applied to x-ray microtomography images from triaxial compression tests on argillaceous rock, Strain 43 (2007) 193–205.
[40] F. Forsberg, M. Sjödahl, R. Mooser, E. Hack, P. Wyss, Full three-dimensional strain measurements on wood exposed to three-point bending: Analysis by use of digital volume correlation applied to synchrotron radiation micro-computed tomography image data, Strain 46 (2010) 47–60.
[41] S. Roux, F. Hild, P. Viot, D. Bernard, Three-dimensional image correlation from x-ray computed tomography of solid foam, Composites Part A: Applied science and manufacturing 39 (2008) 1253–1265.
[42] A. N. Tikhonov, Solution of incorrectly formulated problems and the regularization methods, in: Soviet Mathematics Doklady, volume 4, 1963, pp. 1035–1038.
[43] A. N. Tikhonov, V. Y. Arsenin, Solutions of ill-posed problems, New York (1977) 1–30.
[44] B. K. P. Horn, B. G. Schunck, Determining optical flow, Artif. Intell. 17 (1981) 185–203.
[45] T. Poggio, V. Torre, C. Koch, Computational vision and regularization theory, nature 317 (1985) 314–319.
[46] H. Leclerc, J.-N. Périé, S. Roux, F. Hild, Voxel-scale digital volume correlation, Experimental Mechanics 51 (2011) 479–490.
[47] R. Bajcsy, S. Kovačič, Multiresolution elastic matching, Computer vision, graphics, and image processing 46 (1989) 1–21.
[48] J. Kybic, M. Unser, Fast parametric elastic image registration, IEEE transactions on image processing 12 (2003) 1427–1442.
[49] P. Ruhnau, A. Stahl, C. Schnörr, Variational estimation of experimental fluid flows with physics-based spatio-temporal regularization, Measurement Science and Technology 18 (2007) 755.
[50] N. P. van Dijk, D. Wu, C. Persson, P. Isaksson, A global digital volume correlation algorithm based on higher-order finite elements: Implementation and evaluation, International Journal of Solids and Structures 168 (2019) 211 – 227.
[51] A. Patera, S. Carl, M. Stampanoni, D. Derome, J. Carmeliet, A non-rigid registration method for the analysis of local deformations in the wood cell wall, Advanced Structural and Chemical Imaging 4 (2018) 1.
[52] J. Réthoré, S. Roux, F. Hild, An extended and integrated digital image correlation technique applied to the analysis of fractured samples, European Journal of Computational Mechanics 18 (2009) 285–306.
[53] J.-J. Orteu, D. Garcia, L. Robert, F. Bugarin, A speckle texture image generator, in: Speckle06: speckles, from grains to flowers, volume 6341, International Society for Optics and Photonics, 2006, p. 63410H.
[54] W. E. Lorensen, H. E. Cline, Marching cubes: A high resolution 3d surface construction algorithm, Computer Graphics 21 (1987) 163–169.
[55] O. M. Hafez, Robust Image-Based Modeling and Simulation in Biomechanics, University of California, Davis, 2018.
[56] S. Osher, J. A. Sethian, Fronts propagating with curvature-dependent speed: Algorithms based on hamilton-jacobi formulations, Journal of Computational Physics 79 (1988) 12 – 49.
[57] T. Chan, L. Vese, Active contours without edges, IEEE Transactions on Image Processing 10 (2001) 266–277.
[58] O. Bernard, D. Friboulet, P. Thevenaz, M. Unser, Variational b-spline level-set: A linear filtering approach for fast deformable model evolution, IEEE Transactions on Image Processing 18 (2009) 1179–1191.
[59] L. Piegl, W. Tiller, The NURBS Book, Monographs in Visual Communication, Springer Berlin Heidelberg, 1996.
[60] N. Sukumar, D. Chopp, N. Moës, T. Belytschko, Modeling holes and inclusions by level sets in the extended finite-element method, Computer Methods in Applied Mechanics and Engineering 190 (2001) 6183 – 6200.
[61] D. Rueckert, L. I. Sonoda, C. Hayes, D. L. G. Hill, M. O. Leach, D. J. Hawkes, Nonrigid registration using free-form deformations: application to breast mr images, IEEE Transactions on Medical Imaging 18 (1999) 712–721.
[62] L. Kudela, N. Zander, S. Kollmannsberger, E. Rank, Smart octrees: Accurately integrating discontinuous functions in 3d, Computer Methods in Applied Mechanics and Engineering 306 (2016) 406 – 426.
[63] B. Müller, F. Kummer, M. Oberlack, Highly accurate surface and volume integration on implicit domains by means of moment-fitting, International Journal for Numerical Methods in Engineering 96 (2013) 512–528.
[64] A. Abedian, J. Parvizian, A. Düster, H. Khademyzadeh, E. Rank, Performance of different integration schemes in facing discontinuities in the finite cell method, International Journal of Computational Methods 10 (2013) 1350002.
[65] M. Joulaian, S. Hubrich, A. Düster, Numerical integration of discontinuities on arbitrary domains based on moment fitting, Computational Mechanics 57 (2016) 979–999.
[66] The CGAL Project, CGAL User and Reference Manual, 4.14 ed., CGAL Editorial Board, 2019.
[67] M. Dauge, A. Düster, E. Rank, Theoretical and numerical investigation of the finite cell method, Journal of Scientific Computing 65 (2015) 1039–1064.
[68] M. Ruess, D. Schillinger, Y. Bazilevs, V. Varduhn, E. Rank, Weakly enforced essential boundary conditions for nurbs-embedded and trimmed nurbs geometries on the basis of the finite cell method, International Journal for Numerical Methods in Engineering 95 (2013) 811–846.
[69] C. Lehrenfeld, High order unfitted finite element methods on level set domains using isoparametric mappings, Computer Methods in Applied Mechanics and Engineering 300 (2016) 716 – 733.
[70] M. H. Sadd, Elasticity: theory, applications, and numerics, Academic Press, 2009.
[71] T. S. Newman, H. Yi, A survey of the marching cubes algorithm, Computers & Graphics 30 (2006) 854 – 879.
[72] G. Besnard, F. Hild, S. Roux, "Finite-element" displacement fields analysis from digital images : application to Portevin-Le Châtelier bands, Experimental Mechanics 46 (2006) 789–804.

[73] F. Hild, S. Roux, Comparison of local and global approaches to digital image correlation, Experimental Mechanics 52 (2012) 1503–1519.
[74] N. Roma, J. Santos-Victor, J. Tomé, A comparative analysis of cross-correlation matching algorithms using a pyramidal resolution approach, in: Empirical Evaluation Methods in Computer Vision, World Scientific, 2002, pp. 117–142.
[75] R. Fedele, L. Galantucci, A. Ciani, Global 2d digital image correlation for motion estimation in a finite element framework: a variational formulation and a regularized, pyramidal, multi-grid implementation, International Journal for Numerical Methods in Engineering 96 (2013) 739–762.
[76] J.-C. Passieux, R. Bouclier, Classic and inverse compositional gauss-newton in global dic, International Journal for Numerical Methods in Engineering 119 (2019) 453–468.
[77] R. cai Yang, A regularized finite-element digital image correlation for irregular displacement field, Optics and Lasers in Engineering 56 (2014) 67 – 73.
[78] H. Leclerc, J.-N. Périé, F. Hild, S. Roux, Digital volume correlation: what are the limits to the spatial resolution?, Mechanics & Industry 13 (2012) 361–371.
[79] J. Neggers, B. Blaysat, J. P. M. Hoefnagels, M. G. D. Geers, On image gradients in digital image correlation, International Journal for Numerical Methods in Engineering 105 (2016) 243–260.
[80] J.-E. Pierré, J.-C. Passieux, J.-N. Périé, F. Bugarin, L. Robert, Unstructured finite element-based digital image correlation with enhanced management of quadrature and lens distortions, Optics and Lasers in Engineering 77 (2016) 44–53.
[81] R. Bajcsy, S. Kovačič, Multiresolution elastic matching, Computer Vision, Graphics, and Image Processing 46 (1989) 1 – 21.
[82] E. Haber, J. Modersitzki, A multilevel method for image registration, SIAM Journal on Scientific Computing 27 (2006) 1594–1607.
[83] J. Feydy, B. Charlier, F.-X. Vialard, G. Peyré, Optimal transport for diffeomorphic registration, in: Medical Image Computing and Computer Assisted Intervention - MICCAI 2017, Springer International Publishing, 2017, pp. 291–299.
[84] M. J. Borden, M. A. Scott, J. A. Evans, T. J. R. Hughes, Isogeometric finite element data structures based on bézier extraction of nurbs, International Journal for Numerical Methods in Engineering 87 (2011) 15–47.
[85] D. D'Angella, S. Kollmannsberger, E. Rank, A. Reali, Multi-level bézier extraction for hierarchical local refinement of isogeometric analysis, Computer Methods in Applied Mechanics and Engineering 328 (2018) 147 – 174.
[86] U. Ascher, E. Haber, Grid refinement and scaling for distributed parameter estimation problems, Inverse Problems 17 (2001) 571.
[87] G. Colantonio, M. Chapelier, R. Bouclier, J.-C. Passieux, E. Marenić, Noninvasive multilevel geometric regularization of mesh-based three-dimensional shape measurement, International Journal for Numerical Methods in Engineering 121 (2020) 1877–1897.
[88] F. E. Boas, D. Fleischmann, Ct artifacts: causes and reduction techniques, Imaging in medicine 4 (2012) 229–240.
[89] S. Kleinendorst, J. Hoefnagels, M. Geers, Mechanical shape correlation: A novel integrated digital image correlation approach, Computer Methods in Applied Mechanics and Engineering 345 (2019) 983 – 1006.
[90] J. Réthoré, A fully integrated noise robust strategy for the identification of constitutive laws from digital images, International Journal for Numerical Methods in Engineering 84 (2010) 631–660.
[91] J. Réthoré, Muhibullah, T. Elguedj, M. Coret, P. Chaudet, A. Combescure, Robust identification of elasto-plastic constitutive law parameters from digital images using 3d kinematics, International Journal of Solids and Structures 50 (2013) 73 – 85.
[92] M. Unser, Splines: a perfect fit for signal and image processing, IEEE Signal Processing Magazine 16 (1999) 22–38.
[93] J.-C. Passieux, J.-N. Périé, M. Salaün, A dual domain decomposition method for finite element digital image correlation, International Journal for Numerical Methods in Engineering 102 (2015) 1670–1682.
[94] R. Bouclier, J.-C. Passieux, A domain coupling method for finite element digital image correlation with mechanical regularization: Application to multiscale measurements and parallel computing, International Journal for Numerical Methods in Engineering 111 (2017) 123–143.
[95] J.-C. Passieux, J.-N. Périé, High resolution digital image correlation using proper generalized decomposition: Pgd-dic, International Journal for Numerical Methods in Engineering 92 (2012) 531–550.
[96] J.-C. Passieux, R. Bouclier, J.-N. Périé, A Space-Time PGD-DIC Algorithm, Experimental Mechanics 58 (2018) 1195–1206.
[97] J. N. Jomo, N. Zander, M. Elhaddad, A. Özcan, S. Kollmannsberger, R.-P. Mundani, E. Rank, Parallelization of the multi-level hp-adaptive finite cell method, Computers & Mathematics with Applications 74 (2017) 126 – 142. 5th European Seminar on Computing ESCO 2016.
[98] J. Jomo, F. de Prenter, M. Elhaddad, D. D'Angella, C. Verhoosel, S. Kollmannsberger, J. Kirschke, V. Nübel, E. van Brummelen, E. Rank, Robust and parallel scalable iterative solutions for large-scale finite cell analyses, Finite Elements in Analysis and Design 163 (2019) 14 – 30.